ABSTRACT

Title of dissertation: CAPTURING MICRO-EMULSIONS AND MICRO-FOAMS WITH THE ARBITRARY LAGRANGIAN EULERIAN METHOD

Andrew Brandon, Doctor of Philosophy, 2015

Dissertation directed by: Professor Konstantina Trivisa
Department of Mathematics

The goal of this work is to develop a 2D, heterogenous model for the purpose of studying liquid drainage from micro-foams and micro-emulsions. Liquid drainage within foams and emulsions is an important phenomenon because it affects several intrinsic properties of foams and emulsions, including their viscoelastic and thermophysical properties. While previous attempts have explained some aspects of drainage with a homogenous treatment, there are fundamental questions regarding drainage that remain unanswered.

In our heterogenous model, we treat the bubbles and droplets of micro-foams and micro-emulsions as rigid particles because their small radii result in large surface tension forces, which cause them to remain spherical for a significant portion of time. To track the sharp, rigid interfaces of the droplets and bubbles, we build our heterogenous model upon the Arbitrary Lagrangian Eulerian (ALE) method. The ALE method is a moving grid method that can be expensive because the finite element matrices must be reassembled each time the grid is moved and grid

deformation can lead to low quality elements. We reduce the cost of running ALE simulations by employing a second order accurate, semi-implicit-explicit time integration scheme designed for low Reynolds number flows and by utilizing a novel function for controlling the deformation of the mesh.

With this heterogenous model, we first investigate coarsening induced drainage within an idealized micro-foam. Our heterogenous model shows that the foam's liquid channel thicknesses must be allowed to vary with time in the bubble's coarsening equations. In addition, our model also shows that bubble position is as important as bubble size when it comes to the coarsening process. We conclude this work with a series of studies designed to determine the algorithm's ability to capture the bubbles and droplets of micro-foams and micro-emulsions as a collection of free bodies. The results of this testing indicate that our algorithm is capable of capturing a micro-emulsion as a collection of free body droplets. However, the testing also indicates that our algorithm is not capable of capturing micro-foams as a collection of free body bubbles at this time.

CAPTURING MICRO-EMULSIONS AND MICRO-FOAMS WITH THE ARBITRARY LAGRANGIAN EULERIAN METHOD

by

Andrew Brandon

Dissertation submitted to the Faculty of the Graduate School of the
University of Maryland, College Park in partial fulfillment
of the requirements for the degree of
Doctor of Philosophy
2015

Advisory Committee:
Professor Konstantina Trivisa, Chair/Advisor
Dr. Ramagopal Ananth, Co-Advisor
Professor Maria Cameron
Professor Doron Levy
Professor Panagiotis Dimitrakopoulos

Acknowledgments

I'd like to begin by thanking my advisor Dr. Ramagopal Ananth, for taking me on four years ago. We have worked on several interesting and extremely challenging projects together and the opportunity to do so has been invaluable to me. He has always encouraged me to explore my own ideas and made himself available for help whenever I have asked. It has been a pleasure to work with and learn from him.

I would also like to thank my co-advisor, Professor Konstantina Trivisa. She has been an enormous help throughout the entire process of preparing this manuscript. In addition, she has been a guiding force in helping me prepare for and navigate prospects after graduate school. Thanks are also due to Professor Maria Cameron, Professor Doron Levy, and Professor Panagiotis Dimitrakopoulos for serving on my dissertation committee and reviewing this manuscript.

My colleagues at the Naval Research Laboratory in Washington, D.C. deserve special mention, especially Dr. Michael Conroy, Dr. James Fleming, and Dr. Harold Ladouceur. Their guidance and mentoring played a critical role in the completion of this thesis. I'd also like to thank Dr. Brad Williams, Dr. Ravi Ramamurti, and Katie Hinnant for their help.

I owe my deepest thanks to my family and my wife, Jamie. They have always stood by me throughout my graduate studies, even when my heart was not fully in it, lending a helping hand and words of encouragement. Their support and assistance has made this possible.

I also owe an immense amount of gratitude to my friends within the AMSC

program at the University of Maryland. Without them, things would have been much more difficult at times and I am not sure that I would have had the courage to see things through to the end. Thank you for everything.

Finally, I would like to acknowledge the financial support I have received from the Office of Naval Research and University of Maryland throughout the course of my graduate studies.

I may have inadvertently left some people out, but please know that your assistance was and is much appreciated.

Dedication

To Jamie and my family.

Table of Contents

List of Figures

List of Variables

Roman Letters:

a	Wave amplification factor	$[1/s]$
a_1	Time integration stencil coefficient	$[1/s]$
a_2	Time integration stencil coefficient	$[1/s]$
a_3	Time integration stencil coefficient	$[1/s]$
A	Element area (volume) in 2D (3D)	$[m^2]$
A_a	Apparent area between Bubbles 1 and 2	$[m^2]$
A_b	Apparent area between Bubbles 2 and 3	$[m^2]$
A_B	Area of the cylinder	$[m^2]$
A_i	Area of Bubble i	$[m^2]$
b	Extrapolation stencil coefficient	[unitless]
c	Extrapolation stencil coefficient	[unitless]
c_a	Concentration of dissolved gas in water between Bubbles 1 and 2	$[mol/m^3]$
c_b	Concentration of dissolved gas in water between Bubbles 2 and 3	$[mol/m^3]$
c_i	Concentration of dissolved gas in water surrounding Bubble i	$[mol/m^3]$
C_D	Drag coefficient	[unitless]
C_F	Viscous drag coefficient	[unitless]
C_P	Pressure drag coefficient	[unitless]
D	Effective diffusion coefficient for dissolved gas in water	$[m^2/s]$
D_f	Diffusion coefficient for dissolved gas in water	$[m^2/s]$
F_D	Drag force (per unit length)	$[kg/s^2]$
F_P	Pressure drag force (per unit length)	$[kg/s^2]$
F_μ	Viscous drag force (per unit length)	$[kg/s^2]$
$\vec{g}$	Gravity vector	$[m/s^2]$
H	Measured height of the foam's drained liquid	[m]
He	Henry's constant	$[mol/m^3 \cdot Pa]$
i	Indicator (numeric)	[unitless]
k_e	Mesh deformation function	[unitless]
k_m	Wave number	$[1/m]$
l	Length of an element's side	[m]
L	Element node locations	[m]
L_B	Length of the bubbles	[m]
n	Timestep indicator	[unitless]
$\vec{n}$	Normal unit vector pointing into the cylinder	[m]
P_i	Bubble i's internal pressure	[Pa]
$\mathscr{P}$	Dynamic pressure	[Pa]
Q	Element quality	[unitless]
r	Timestep ratio	[unitless]
r_u	Stress integral (u component) in weak form	$[kg \cdot m^2/s]$
r_v	Stress integral (v component) in weak form	$[kg \cdot m^2/s]$
r_B	Radius of the cylinder	[m]
R	Average bubble radius	[m]

R_i	Radius of Bubble i	[m]
Re	Reynolds number	[unitless]
Re_m	Reynolds mesh number	[unitless]
Re_m^{crit}	Critical Reynolds mesh number	[unitless]
u	Horizontal component of $\vec{U}$	[m/s]
u_i	Horizontal velocity of Bubble i	[m/s]
$\vec{U}$	Velocity of the surrounding fluid	[m/s]
U_{max}	Characteristic maximum velocity	[m/s]
v	Vertical component of $\vec{U}$	[m/s]
v_i	Vertical velocity of Bubble i	[m/s]
$\vec{V}$	Translational velocity of the cylinder	[m/s]
V_∞	Unidirectional free stream flow velocity component	[m/s]
V_m	Molar volume constant	[mol/m^3]
V_T	Terminal velocity of the cylinder	[m/s]
w_u	Horizontal component of $\vec{W}$	[m/s]
w_v	Vertical component of $\vec{W}$	[m/s]
$\vec{W}$	Grid velocity	[m/s]
X	Stationary (Eulerian) coordinate	[m]
$\vec{X}$	Interfacial grid point locations	[m]
$\vec{X}_c$	Centroid of the cylinder	[m]

Greek Letters:

α	Diffusive CFL number	[unitless]
β	Convective CFL number	[unitless]
γ	Surface tension	[N/m]
Γ	Boundary of the cylinder	[m]
Δt	Timestep	[s]
Δx	Grid node spacing	[m]
ε	Constant film thickness	[m]
θ	Polar angle formed by view factor	[rad]
θ_i	Vector of polar angles formed by the boundary nodes on Bubble i	[rad]
Θ	Growth factor	[unitless]
κ	Foam's liquid fraction	[unitless]
λ_a	Film thickness between Bubbles 1 and 2	[m]
λ_a^0	Initial film thickness between Bubbles 1 and 2	[m]
λ_b	Film thickness between Bubbles 2 and 3	[m]
λ_b^0	Initial film thickness between Bubbles 2 and 3	[m]
μ	Dynamic viscosity of the surrounding fluid	[kg/m·s]
ν	Kinematic viscosity of the surrounding fluid	[m^2/s]
ξ	Ratio of channel width (W) to droplet diameter (d)	[unitless]
ρ	Density of the surrounding fluid	[kg/m^3]

ρ_B	Density of the cylinder	$[\mathrm{kg}/\mathrm{m}^3]$
τ	Viscous stress tensor	$[\mathrm{kg}/\mathrm{m}\cdot\mathrm{s}^2]$
ϕ	Quadratic velocity test function	$[\mathrm{m}/\mathrm{s}]$
χ	Referential (ALE) coordinate	$[\mathrm{m}]$
ψ	Linear pressure test function	$[\mathrm{kg}/\mathrm{m}\cdot\mathrm{s}^2]$
$\vec{\omega}$	Rotational velocity of the cylinder	$[1/\mathrm{s}]$
Ω	Domain's location	$[\mathrm{m}]$

List of Abbreviations

ALE	Arbitrary Lagrangian Eulerian
BDEX2	Semi-Implicit-Explicit Time Integration Scheme
CFL	Courant-Friedrichs-Lewy
CPU	Central Processing Unit
NRL	Naval Research Laboratory
PE(CE)^k	Predictor-Corrector Method with k corrector steps

Chapter 1: Introduction

1.1 Multiphase Flows

Multiphase flows are present all around us and they directly affect our everyday life. Examples of multiphase flows include soil sedimentation in rivers, droplet deformation in sprays, and liquid drainage in emulsions and foams. These flows have impacts ranging from inkjet printing to waterway dredging and from gold mining to automobile safety. Because of the great significance of these flows in practical applications, many attempts have been made to investigate them.

Within these attempts, a homogeneous approach has typically been taken and the multiphase media is assumed to be a continuum. While some insights can be gained from homogeneous approaches, more meaningful results are gained from studies that take a heterogeneous approach and distinguish between phases. Still, there are a limited number of heterogeneous media models within the current literature [6, 16, 27]. As such, homogeneous media models remain the cutting edge technique in numerous multiphase problems, such as liquid drainage in foams and emulsions [26].

Drainage is an important phenomenon because it affects several intrinsic properties of aqueous foams and emulsions. This is due to the fact that the amount of

water within a foam or emulsion directly influences how that foam or emulsion behaves as a media. For example, drainage impacts the effective thermal conductivity, density, heat capacity, viscosity, and gas diffusivity of foams and emulsions, which govern the heat, mass, and momentum transport in the foams and emulsions. With regards to fire fighting foams, these drainage impacts play a significant role in determining whether or not a fire can be successfully extinguished.

Despite a rich amount of literature on the subject, homogeneous media models have left several fundamental questions regarding drainage and its effects open. The goal of this work is to make significant advances towards the creation of a heterogenous media model for the purpose of studying local liquid drainage in micro-foams and micro-emulsions in order to answer some of these open fundamental questions.

1.2 The Arbitrary Lagrangian Eulerian Method

The heterogenous model of drainage under consideration is based upon the 2D incompressible Navier-Stokes equations and the Arbitrary Lagrangian Eulerian (ALE) method. The ALE method is a moving mesh method that was devised in the 1960's, however, it wasn't until the work done in the 1970's by C. W. Hirt and his Los Alamos research group, that the ALE method's true potential was realized [19]. Since then, the ALE method has successfully been applied to several multiphase problems and has gained popularity within the multiphase community because it combines the ability of the Eulerian frame to handle grid distortions with the ability

of the Lagrangian frame to accurately track sharp interfaces [6, 16, 27]. The ALE method does this by employing the referential frame and moving the boundary grid points with a specific velocity. On moving boundaries, the grid points move with the interfacial velocity, while those on stationary boundaries remain fixed. Interior grid points are allowed to move with an arbitrary velocity. By moving the grid points in such a fashion, the moving interfaces are treated in the Lagrangian frame, allowing for sharp interface tracking, while the stationary boundaries are treated in the Eulerian frame, allowing for a moderate degree of grid distortion to be handled.

Though the ALE method allows for an accurate treatment of moving interfaces, it subjects simulations to some of the limitations common to Lagrangian simulations. Specifically, the finite element matrices must be reassembled each time the grid moves. This process can be very expensive and typical ALE algorithms only exacerbate this cost. This is because low accuracy time integration schemes are employed, which necessitate the use of iterative solvers to find the domain's location at the next timestep, Ω^{n+1}. After each iteration in which the grid is moved, reassembly is required, regardless of whether or not the simulation is moving forward in time.

We build our heterogeneous drainage model by designing an ALE algorithm that does not require iterative methods to find Ω^{n+1}. This is accomplished by incorporating a second order accurate time integration scheme into the model. In addition, we seek to reduce the cost of remeshing, due to grid distortion, by limiting the distortion itself. This is accomplished by devising a novel function to control the deformation of the mesh, which in turn reduces the frequency of remeshing. Together, these two aspects significantly reduce the simulation's CPU time over

previous codes, without a loss of accuracy.

1.3 Bubbles and Droplets as Rigid Cylinders

To capture the micro-bubbles and micro-droplets within this heterogeneous drainage model, we employ a no-slip, rigid particle boundary condition to represent the surfaces of the bubbles and droplets. This is a reasonable boundary condition because the radii of the bubbles and droplets that comprise the foams and emulsions under investigation are between 10^{-3}m and 10^{-4}m. On this scale, the surface tension force is so large that the bubbles and droplets remain spherical for a significant portion of time, which was confirmed by experimental observation. Since we have a 2D model, these rigid, spherical bubbles and droplets are approximated by infinite cylinders.

In general, the no-slip, rigid particle boundary condition takes the form

$$\vec{U} = \vec{V} + \vec{\omega} \times (\vec{X} - \vec{X}_c) \tag{1.1}$$

where $\vec{U}$, $\vec{V}$, $\vec{\omega}$, $\vec{X}$, and $\vec{X}_c$ represent the velocity of the fluid surrounding the particle, the translational velocity of the particle, the rotational velocity of the particle, the interfacial grid point locations, and the particle's centroid respectively [14, 16]. Equation 1.1 is a 3D expression and despite the model being in 2D, it is kept in its general, 3D form. This is because the entries corresponding to the additional dimension are identical to 0 in 2D and are ignored after the cross products are taken.

For rigid, infinite cylinders in 2D, the equations governing $\vec{V}$ and $\vec{\omega}$ can be

simplified to

$$\frac{d\vec{V}}{dt} = \left(\frac{\rho_B - \rho}{\rho_B}\right)\vec{g} + \left(\frac{1}{\rho_B A_B}\right)\int_\Gamma \left(\mathscr{P}\vec{n} + \tau\cdot\vec{n}\right) d\Gamma \tag{1.2}$$

and

$$\frac{d\vec{\omega}}{dt} = \left(\frac{2}{\rho_B A_B r_B^2}\right)\int_\Gamma \left(\vec{X} - \vec{X}_c\right)\times\left(\mathscr{P}\vec{n} + \tau\cdot\vec{n}\right) d\Gamma, \tag{1.3}$$

while still allowing the general form of Equation 1.1 to be employed [3, 4, 14, 16]. Within Equations 1.2 and 1.3, ρ is the density of the surrounding fluid, ρ_B is the density of the cylinder, $\mathscr{P}$ is the fluid's dynamic pressure, τ is the fluid's viscous stress tensor, A_B is the area of the cylinder, r_B is the cylinder's radius, $\vec{g}$ is the gravity vector, $\vec{n}$ is the normal unit vector pointing into the cylinder, and Γ represents the cylinder's boundary. These equations have been used extensively in sedimentation studies and we refer the reader to [9, 11, 14–16].

The challenge in coupling Equations 1.2 and 1.3 to the incompressible Navier-Stokes equations is that when ρ_B becomes small with respect to ρ, the terms on the right hand side of Equations 1.2 and 1.3 become large, which causes the overall system to become stiff. This has limited the range of the ρ_B and ρ values that have previously been explored with Equation 1.1. To further advance our heterogenous drainage model, the algorithm is tailored to allow new regions of ρ_B to be explored. This is accomplished by including a predictor-corrector scheme that iterates upon $\mathscr{P}$, τ, $\vec{V}$, and $\vec{\omega}$, but not Ω^{n+1}. This maintains the reassembly cost savings while mitigating the stiffness from the ρ_B^{-1} terms in Equations 1.2 and 1.3.

The main contributions of this work to the existing ALE literature are made possible by our algorithm. Specifically, by reducing the cost of ALE simulations,

we are able to investigate coarsening induced drainage in foams, and by mitigating the rigid particle boundary condition stiffness, we are able to study new regimes of rigid cylinders. These advances have allowed us to draw important conclusions about coarsening, all while moving closer to the creation of a heterogenous, free body model of micro-foams and micro-emulsions. Upon completion of such a model, a successful, comprehensive investigation of drainage in micro-foams and micro-emulsions would be possible.

1.4 Outline of Thesis

In Chapter 2, we discuss the two-dimensional, incompressible Navier-Stokes equations that govern our ALE systems. We begin with the conservation of mass and momentum equations, apply our system assumptions, and translate the equations into the referential frame. Once the governing equations have been discussed, their weak form is presented. The semi-implicit-explicit time integration scheme that we employ to solve the weak form of the incompressible Navier-Stokes equations is then described. Time-step analysis of the scheme, with new results, is also provided. The chapter concludes with an in-depth review of the algorithm. This review includes an exploration into how the grid is moved and how the grid deformation is controlled.

In Chapter 3, we present several validation studies that are performed on our algorithm and its implementation. The validation studies can be separated into two categories. The first set of studies are based on a time dependent, analytical solution to the incompressible Navier-Stokes equations. Comparing numerical results to this

analytical solution is a popular method for benchmarking codes [21, 23]. We extend this method to the ALE framework and use it to investigate the algorithm's ability to accurately track interfaces as well as to confirm the accuracy of our algorithm. The second set of studies take into account the coupling of Equations 1.2 and 1.3 to the incompressible Navier-Stokes equations. The studies begin by examining the code's ability to accurately predict drag coefficients for a stationary cylinder exposed to free stream flows and flows within a channel. In the next study, the cylinder is made buoyant and the fluid's dynamic viscosity, μ, is varied. For each value of μ tested, the cylinder is allowed to reach its terminal velocity, V_T. The numerical solutions for V_T are then compared to an empirical approximation [11, 25]. The purpose of this set of studies is to confirm our code's ability to model buoyant and leaden droplets and bubbles.

In Chapter 4, one of the fundamental questions regarding foams, drainage due to coarsening, is investigated. Coarsening is the process where larger foam bubbles grow at the cost of smaller bubbles. This can have a significant effect on drainage. We create a local model of an idealized foam and derive the rates of coarsening for each bubble. With these rate of coarsening equations, local interstitial fluid flow is induced and constant versus varying film thicknesses are investigated. To determine whether constant or varying film thicknesses more accurately represent the local drainage process, the model results are compared to experimental drainage data from [17]. Then, the importance of bubble size and position with regards to coarsening are investigated with our idealized foam and coarsening equations.

In Chapter 5, two performance studies, whose purposes are to determine our

model's capabilities with regards to ρ_B, are run. The first test involves running simulations, with ever decreasing values of ρ_B, out to steady state until decreasing ρ_B further makes finding the steady state prohibitively expensive. This investigation is parallel in nature to the final validation test and its purpose is to highlight the buoyant regimes that we are able to model for an extended period of time with our current computational resources. Of course, computational resources are always increasing and just because modeling smaller bubble densities is too expensive today does not mean that they will be in the future. To put a lower bound on the bubble densities that the code can handle, ρ_B is further decreased in the second application. For each ρ_B tested within this study, the simulations are run until the solution's stability is not in question. Once stability becomes an issue, the study concludes. We determine the contributions that our model makes by comparing the results of these tests to the results from other published works.

Chapter 6 provides the conclusion to this dissertation.

Chapter 2: Governing Equations and Algorithm

The investigation of drainage in foams and emulsions requires the accurate resolution of the low Reynolds number fluid flow that occurs within the liquid channels. This is because the flow surrounding the bubbles and droplets directly affects the interfacial positions when Equations 1.2 and 1.3 are invoked. Without an accurate calculation of the stress field, the interfacial positions and model's results become questionable, even when the ALE method is being utilized.

2.1 ALE Conservation Equations

The flow that takes place in the liquid channels is governed by the conservation of mass and momentum equations. These equations, for a viscous, compressible, Newtonian fluid in the Eulerian frame, are represented by

$$\rho \frac{\partial \vec{U}}{\partial t}\Big|_X + \rho \vec{U} \cdot \nabla \vec{U} + \nabla \mathscr{P} = -\nabla \cdot \tau \tag{2.1}$$

and

$$\frac{\partial \rho}{\partial t}\Big|_X + \vec{U} \cdot \nabla \rho = -\rho \nabla \cdot \vec{U}, \tag{2.2}$$

[3, 4]. The term $|_X$ on the time derivative in Equations 2.1 and 2.2 is meant to highlight the fact that the time derivative is taken with the stationary coordinate,

X, fixed in time.

Translating Equations 2.1 and 2.2 from the stationary frame to the referential frame can be easily accomplished by utilizing the well known relationship

$$\frac{\partial f}{\partial t}\Big|_X + \vec{U} \cdot \nabla f = \frac{\partial f}{\partial t}\Big|_\chi + (\vec{U} - \vec{W}) \cdot \nabla f \tag{2.3}$$

presented in [7]. The left hand side of Equation 2.3 represents the material derivative of a function f in the stationary frame, while the right hand side represents the material derivative of f in the referential frame, χ. The term $|_\chi$ on the time derivative in Equation 2.3 signifies that the time derivative is taken with χ fixed in time. The referential frame moves with an arbitrary velocity, $\vec{W}$. Note that by specifying the frame velocity $\vec{W}$ to be $\vec{0}$, the Eulerian frame is recovered. Similarly, the Lagrangian frame can be recovered by setting $\vec{W}$ to be $\vec{U}$. For this reason, the referential frame's material derivative is said to take an Arbitrary Lagrangian Eulerian form.

By letting f equal ρ in Equation 2.3, the Eulerian material derivative in Equation 2.2 can be replaced with the ALE material derivative. Similarly, by letting f equal $\vec{U}$ in Equation 2.3 and multiplying by ρ, the Eulerian material derivative in Equation 2.1 can be replaced with the ALE material derivative. These substitutions result in

$$\rho\frac{\partial \vec{U}}{\partial t}\Big|_\chi + \rho(\vec{U} - \vec{W}) \cdot \nabla\vec{U} + \nabla\mathscr{P} = -\nabla \cdot \tau \tag{2.4}$$

and

$$\frac{\partial \rho}{\partial t}\Big|_\chi + (\vec{U} - \vec{W}) \cdot \nabla\rho = -\rho\nabla \cdot \vec{U}, \tag{2.5}$$

which represent the conservation of mass and momentum equations in the ALE form.

At this point we assume that the fluid is incompressible and has a constant dynamic viscosity, μ. This simplifies Equation 2.5 to

$$\nabla \cdot \vec{U} = 0 \tag{2.6}$$

and allows τ to be written as $\tau = -\mu(\nabla\vec{U} + \nabla\vec{U}^T)$ [3, 4]. Note that the expression $\nabla \cdot \tau$ can be further reduced to $-\mu\nabla^2\vec{U}$ using the above assumptions, but that simplification is not made here because the term $\nabla \cdot \tau$ is needed in the weak form. By substituting $\vec{U} = [u, v]$, $\vec{W} = [w_u, w_v]$, and $\tau = -\mu(\nabla\vec{U} + \nabla\vec{U}^T)$, Equations 2.4 and 2.6 can be written in 2D Cartesian coordinates as

$$\rho\frac{\partial u}{\partial t}\Big|_\chi + \rho(u-w_u)\frac{\partial u}{\partial x}+\rho(v-w_v)\frac{\partial u}{\partial y}+\frac{\partial \mathscr{P}}{\partial x} = \mu\left[\frac{\partial}{\partial x}\Big(2\frac{\partial u}{\partial x}\Big)+\frac{\partial}{\partial y}\Big(\frac{\partial u}{\partial y}+\frac{\partial v}{\partial x}\Big)\right], \tag{2.7}$$

$$\rho\frac{\partial v}{\partial t}\Big|_\chi + \rho(u-w_u)\frac{\partial v}{\partial x}+\rho(v-w_v)\frac{\partial v}{\partial y}+\frac{\partial \mathscr{P}}{\partial y} = \mu\left[\frac{\partial}{\partial x}\Big(\frac{\partial u}{\partial y}+\frac{\partial v}{\partial x}\Big)+\frac{\partial}{\partial y}\Big(2\frac{\partial v}{\partial y}\Big)\right], \tag{2.8}$$

and

$$\frac{\partial u}{\partial x} + \frac{\partial v}{\partial y} = 0 \tag{2.9}$$

which represent our model equations in component form.

2.2 Weak Formulation

To ensure a solution for u, v, and $\mathscr{P}$ can be found, the finite element spaces that are used in the weak form must be chosen in such a way that the Babuška-Brezzi condition is satisfied [18]. There are several combinations of finite element spaces that satisfy the Babuška-Brezzi condition, but the combination we use corresponds to the triangular Taylor-Hood element. The reasons for this are twofold. First, having a quadratic velocity function and a linear pressure function provide the

necessary balance between accuracy and computational cost. Second, the multi-scale flows we are studying with this code often reach the regime of lubrication at several locations within the domain. Because the Taylor-Hood elements are quadratic with respect to velocity, a single element can provide the exact solution for velocity in these locations. Of course, the grid has a higher density than one element in these locations, but the use of Taylor-Hood elements allows for a coarser mesh than other, less accurate elements would require.

Let ϕ_i denote the quadratic velocity test function and let ψ_i denote the linear pressure test function in the Taylor-Hood element. By multiplying Equations 2.7 and 2.8 by ϕ_i and Equation 2.9 by ψ_i, integrating over Ω, and applying integration by parts on the viscous and pressure terms,

$$\int_\Omega \rho \frac{\partial u}{\partial t}\Big|_\chi \phi_i \, d\Omega + \int_\Omega \rho(u - w_u)\frac{\partial u}{\partial x}\phi_i \, d\Omega + \int_\Omega \rho(v - w_v)\frac{\partial u}{\partial y}\phi_i \, d\Omega - \int_\Omega \mathscr{P}\frac{\partial \phi_i}{\partial x} \, d\Omega + \int_\Omega 2\mu \frac{\partial u}{\partial x}\frac{\partial \phi_i}{\partial x} \, d\Omega + \int_\Omega \mu\Big(\frac{\partial u}{\partial y} + \frac{\partial v}{\partial x}\Big)\frac{\partial \phi_i}{\partial y} \, d\Omega = r_u, \tag{2.10}$$

$$\int_\Omega \rho \frac{\partial v}{\partial t}\Big|_\chi \phi_i \, d\Omega + \int_\Omega \rho(u - w_u)\frac{\partial v}{\partial x}\phi_i \, d\Omega + \int_\Omega \rho(v - w_v)\frac{\partial v}{\partial y}\phi_i \, d\Omega - \int_\Omega \mathscr{P}\frac{\partial \phi_i}{\partial y} \, d\Omega + \int_\Omega \mu\Big(\frac{\partial u}{\partial y} + \frac{\partial v}{\partial x}\Big)\frac{\partial \phi_i}{\partial x} \, d\Omega + \int_\Omega 2\mu \frac{\partial v}{\partial y}\frac{\partial \phi_i}{\partial y} \, d\Omega = r_v, \tag{2.11}$$

and

$$\int_\Omega \frac{\partial u}{\partial x}\psi_i \, d\Omega + \int_\Omega \frac{\partial v}{\partial y}\psi_i \, d\Omega = 0 \tag{2.12}$$

follow. The terms r_u and r_v represent the line integrals along Γ that result from the integration by parts. They are represented by

$$r_u = \int_\Gamma \Big(2\mu \frac{\partial u}{\partial x}n_x + \mu\Big(\frac{\partial u}{\partial y} + \frac{\partial v}{\partial x}\Big)n_y - \mathscr{P}n_x\Big)\phi_i \, d\Gamma \tag{2.13}$$

and

$$r_v = \int_\Gamma \Big(\mu\Big(\frac{\partial u}{\partial y} + \frac{\partial v}{\partial x}\Big)n_x + 2\mu\frac{\partial v}{\partial y}n_y - \mathscr{P}n_y\Big)\phi_i \, d\Gamma, \tag{2.14}$$

where n_x and n_y represent the components of the outward unit normal along Γ. Equations 2.10, 2.11, and 2.12 represent the weak form of the non-conservative ALE conservation equations.

2.3 Time Integration Scheme

To solve Equations 2.10, 2.11, and 2.12, a scheme popular in Eulerian codes and designed for low Reynolds number flows is implemented [12]. The scheme is referred to as BDEX2 since it utilizes a second order accurate backwards difference stencil for the time derivative as well as a second order accurate extrapolation stencil for the convection terms. While the convection terms are treated explicitly through extrapolation, the viscous and pressure terms are handled implicitly to remove any timestep restrictions related to viscosity. The reader should be made aware that the BDEX2 scheme has also been referred to as Extrapolated Gear and SBDF within Eulerian codes [1]. Several BDEX schemes, of up to fifth order, are analyzed for the Stokes Equations in the ALE form in [19].

There are two main reasons for using BDEX2. First, handling the convection terms explicitly removes the need for an iterative, nonlinear matrix solver. An explicit treatment of these terms is reasonable because the convection contributions are relatively small in low Reynolds number flows. The second reason is that an iterative solver such as a predictor-corrector scheme, PE(CE)^k, is typically needed

to accurately find Ω at the next timestep, Ω^{n+1}, when low accuracy elements and time discretizations are used [27]. The accuracy of BDEX2 and the Taylor-Hood elements allow Ω^{n+1} to be found accurately in a single step, removing the need to iteratively find Ω^{n+1}.

Allowing for a variable time step, the second order accurate backwards difference approximation of the time derivative at time t^{n+1} takes the form

$$\left.\frac{\partial f}{\partial t}\right|^{n+1} \approx a_1 f^{n+1} + a_2 f^n + a_3 f^{n-1} \tag{2.15}$$

where

$$a_1 = \frac{2\Delta t^n + \Delta t^{n-1}}{(\Delta t^n)^2 + \Delta t^n \Delta t^{n-1}}, \tag{2.16}$$

$$a_2 = -\frac{\Delta t^n + \Delta t^{n-1}}{\Delta t^n \Delta t^{n-1}}, \tag{2.17}$$

and

$$a_3 = \frac{\Delta t^n}{\Delta t^n \Delta t^{n-1} + (\Delta t^{n-1})^2} \tag{2.18}$$

where $\Delta t^n = t^{n+1} - t^n$. Because we are approximating the time derivative at time t^{n+1}, all terms are integrated over Ω^{n+1} in Equations 2.10, 2.11, and 2.12 with the exception of the two terms in the time discretization that relate to past information. These terms are integrated over Ω^n and Ω^{n-1}, respectively [10]. Although the convection terms are treated explicitly using extrapolation, they are integrated over Ω^{n+1}. This is because the purpose of the extrapolation stencil is to approximate the value at time t^{n+1}. The extrapolation stencil used is represented by

$$f^{n+1} \approx \hat{f}^{n+1} = b f^n + c f^{n-1} \tag{2.19}$$

where

$$b = \frac{\Delta t^n + \Delta t^{n-1}}{\Delta t^{n-1}} \tag{2.20}$$

and

$$c = -\frac{\Delta t^n}{\Delta t^{n-1}}. \tag{2.21}$$

Before continuing, it is important to note that $\phi_i \equiv \phi_i(t)$ in the ALE form and the appropriate choice of ϕ_i on Ω^n is ϕ_i^n [10]. Similarly, ψ_i^n is the appropriate choice for ψ_i on Ω^n. This is because both ϕ_i and ψ_i are test functions over Ω. Thus, they must change in time when Ω does. By applying the time discretization and extrapolation stencils as well as choosing ϕ_i and ψ_i at the appropriate times, Equations 2.10, 2.11, and 2.12 become

$$\begin{aligned}
&\int_{\Omega^{n+1}} \rho a_1 u^{n+1}\phi_i^{n+1}\,d\Omega + \int_{\Omega^n} \rho a_2 u^n \phi_i^n\,d\Omega + \int_{\Omega^{n-1}} \rho a_3 u^{n-1}\phi_i^{n-1}\,d\Omega + \\
&\int_{\Omega^{n+1}} \rho(\hat{u}^{n+1} - \hat{w}_u^{n+1})\frac{\partial \hat{u}^{n+1}}{\partial x}\phi_i^{n+1}\,d\Omega + \int_{\Omega^{n+1}} \rho(\hat{v}^{n+1} - \hat{w}_v^{n+1})\frac{\partial \hat{u}^{n+1}}{\partial y}\phi_i^{n+1}\,d\Omega - \\
&\int_{\Omega^{n+1}} \mathscr{P}^{n+1}\frac{\partial \phi_i^{n+1}}{\partial x}\,d\Omega + \int_{\Omega^{n+1}} 2\mu\frac{\partial u^{n+1}}{\partial x}\frac{\partial \phi_i^{n+1}}{\partial x}\,d\Omega + \int_{\Omega^{n+1}} \mu\frac{\partial u^{n+1}}{\partial y}\frac{\partial \phi_i^{n+1}}{\partial y}\,d\Omega + \\
&\int_{\Omega^{n+1}} \mu\frac{\partial v^{n+1}}{\partial x}\frac{\partial \phi_i^{n+1}}{\partial y}\,d\Omega = r_u^{n+1},
\end{aligned} \tag{2.22}$$

$$\begin{aligned}
&\int_{\Omega^{n+1}} \rho a_1 v^{n+1}\phi_i^{n+1}\,d\Omega + \int_{\Omega^n} \rho a_2 v^n \phi_i^n\,d\Omega + \int_{\Omega^{n-1}} \rho a_3 v^{n-1}\phi_i^{n-1}\,d\Omega + \\
&\int_{\Omega^{n+1}} \rho(\hat{u}^{n+1} - \hat{w}_u^{n+1})\frac{\partial \hat{v}^{n+1}}{\partial x}\phi_i^{n+1}\,d\Omega + \int_{\Omega^{n+1}} \rho(\hat{v}^{n+1} - \hat{w}_v^{n+1})\frac{\partial \hat{v}^{n+1}}{\partial y}\phi_i^{n+1}\,d\Omega - \\
&\int_{\Omega^{n+1}} \mathscr{P}^{n+1}\frac{\partial \phi_i^{n+1}}{\partial y}\,d\Omega + \int_{\Omega^{n+1}} \mu\frac{\partial u^{n+1}}{\partial y}\frac{\partial \phi_i^{n+1}}{\partial x}\,d\Omega + \int_{\Omega^{n+1}} \mu\frac{\partial v^{n+1}}{\partial x}\frac{\partial \phi_i^{n+1}}{\partial x}\,d\Omega + \\
&\int_{\Omega^{n+1}} 2\mu\frac{\partial v^{n+1}}{\partial y}\frac{\partial \phi_i^{n+1}}{\partial y}\,d\Omega = r_v^{n+1},
\end{aligned} \tag{2.23}$$

and

$$\int_{\Omega^{n+1}} \frac{\partial u^{n+1}}{\partial x} \psi_i^{n+1} \, d\Omega + \int_{\Omega^{n+1}} \frac{\partial v^{n+1}}{\partial y} \psi_i^{n+1} \, d\Omega = 0, \tag{2.24}$$

respectively. To complete the transformation of Equations 2.7, 2.8 and 2.9, the substitutions

$$u = \sum_j u_{h,j} \phi_j, \tag{2.25}$$

$$v = \sum_j v_{h,j} \phi_j, \tag{2.26}$$

and

$$\mathscr{P} = \sum_k \mathscr{P}_{h,k} \psi_k \tag{2.27}$$

are made in Equations 2.22, 2.23, and 2.24. This results in a system of linear equations governing u_h, v_h, and $\mathscr{P}_h$. Within this spatial discretization, u_h and v_h represent the velocity component values of the j velocity nodes on the Taylor-Hood elements. Similarly, $\mathscr{P}_h$ represents the pressure values of the k pressure nodes on the Taylor-Hood elements.

2.4 BDEX2 Timestep Analysis

As previously discussed, the diffusion terms are treated implicitly in order to remove the timestep restriction that arises from the large viscous terms in these multi-scale problems. However, the resulting timestep restriction is not obvious. Ascher et al. performed timestep analysis on the BDEX2 scheme, but the analysis was only performed using a constant timestep and was limited in scope [1]. To discern how BDEX2 behaves with a non-constant timestep, von Neumann stability

analysis was performed using the following convection-diffusion equation,

$$\frac{\partial u}{\partial t} = -U_{max}\frac{\partial u}{\partial x} + \nu\frac{\partial^2 u}{\partial x^2}. \tag{2.28}$$

Discretizing Equation 2.28 using BDEX2 and second order centered differencing gives

$$a_1 u_i^{n+1} + a_2 u_i^n + a_3 u_i^{n-1} = \frac{U_{max}}{2\Delta x}\Big(b u_{i-1}^n + c u_{i-1}^{n-1} - b u_{i+1}^n - c u_{i+1}^{n-1}\Big) + \frac{\nu}{\Delta x^2}\Big(u_{i+1}^{n+1} - 2u_i^{n+1} + u_{i-1}^{n+1}\Big), \tag{2.29}$$

where the coefficients a_1, a_2, a_3, b, and c are defined as they were originally. By assuming that

$$u_{i+h}^{n+m} = e^{at^{n+m}} e^{ik_m(x+h\Delta x)}, \tag{2.30}$$

Equation 2.29 can be simplified to

$$e^{a(\Delta t^n + \Delta t^{n-1})}\left[a_1 + \frac{2\nu}{\Delta x^2} - \frac{2\nu}{\Delta x^2}\cos(k_m\Delta x)\right] + e^{a\Delta t^{n-1}}\left[a_2 + \frac{U_{max}bi}{\Delta x}\sin(k_m\Delta x)\right] + \left[a_3 + \frac{U_{max}ci}{\Delta x}\sin(k_m\Delta x)\right] = 0. \tag{2.31}$$

Since this relationship must be true for all k_m and Δx, regardless of the sign of U_{max}, the sine functions can be replaced by -1. To avoid canceling the viscous terms, the cosine function is also replaced by -1, instead of 1. Also, define $r = \frac{\Delta t^{n-1}}{\Delta t^n}$. With these two substitutions, Equation 2.31 can be simplified to

$$e^{a\Delta t^n(r+1)}\Big(a_1 + \frac{4\nu}{\Delta x^2}\Big) + e^{a\Delta t^n r}\Big(a_2 - \frac{U_{max}bi}{\Delta x}\Big) + \Big(a_3 - \frac{U_{max}ci}{\Delta x}\Big) = 0. \tag{2.32}$$

Replacing the growth factor, $e^{a\Delta t^n}$, by Θ in Equation 2.32 as well as multiplying by Δt^n gives

$$\Theta^{r+1}\Big(a_1\Delta t^n - \alpha\Big) + \Theta^r\Big(a_2\Delta t^n - \beta bi\Big) + \Big(a_3\Delta t^n - \beta ci\Big) = 0, \tag{2.33}$$

where

$$\alpha = \frac{-4\nu\Delta t^n}{\Delta x^2} \tag{2.34}$$

and

$$\beta = \frac{U_{max}\Delta t^n}{\Delta x}. \tag{2.35}$$

Note that $\frac{-4\beta}{\alpha}$ represents the Reynolds mesh number, Re_m. Equation 2.33 represents the characteristic polynomial of the BDEX2 scheme. Ascher et al. considered the case of a constant timestep, $r = 1$, and in this case, Equation 2.33 matches the characteristic polynomial presented in [1].

In order for BDEX2 to be stable, all of the roots of Equation 2.33 must have a magnitude less than or equal to 1, $|\Theta| \leq 1$. As far as we know, Equation 2.33 does not have an analytical solution for general r. Thus, three basic regimes of r are investigated. The regimes correspond to a constant timestep, $r = 1$, a shrinking timestep, $r = 1.1$, and a growing timestep, $r = 0.9$. With the value of r specified, the $\alpha - \beta$ plane is discretized and the roots of Equation 2.33 are solved numerically on each discretized node. Finally, the magnitude of the roots are taken.

Figure 2.1 depicts the stability region of BDEX2 for $r = 1$. The stability regions for $r = 1.1$ and $r = 0.9$ differ from that of $r = 1$, but only minimally. Because the differences are slight, the results for $r = 1.1$ and $r = 0.9$ will not be discussed further in this manuscript. Ascher et al. presented a figure similar to Figure 2.1, but the range of β was limited. By increasing the scope on the $\alpha - \beta$ plane, an important feature of the BDEX2 scheme can be seen that was not recognized in [1]. As α and β become large, the ridge separating the stability regions becomes linear.

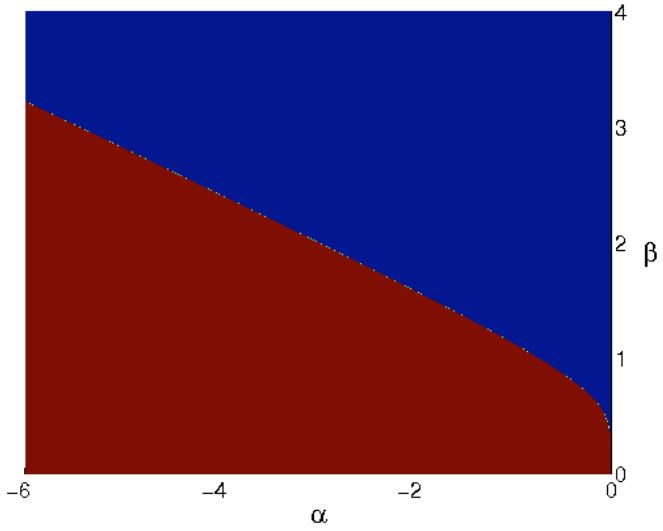

Figure 2.1: Stability region for BDEX2 according to Equation 2.33 with $r = 1$. Red denotes stability and blue denotes instability.

This implies that $\frac{-4\beta}{\alpha}$ remains constant along that linear ridge. This means that BDEX2 is stable for all $Re_m \leq Re_m^{crit}$, where Re_m^{crit} is determined by the slope of the ridge. According to our analysis, Re_m^{crit} is slightly larger than 1.6 for $r = 1$. Thus, when the quantity $U_{max}\Delta x$ is less than 1.6ν, BDEX2 is guaranteed to be stable for any timestep size.

2.5 Grid Deformation

One aspect of this work that has not yet been discussed is the grid velocity $\vec{W}$ and how the grid is moved. The basis of the ALE method is that points on a moving interface move with that interface while points on stationary boundaries remain stationary. These restrictions result in the constraints that $\vec{W} = \vec{U}$ on moving interfaces and $\vec{W} = \vec{0}$ on stationary boundaries. Thus, the grid behaves in a

Lagrangian fashion in the immediate vicinity of moving interfaces and an Eulerian fashion in the immediate vicinity of stationary boundaries. Meanwhile, the interior grid points move at an arbitrary velocity.

The literature provides several methods for specifying the arbitrary interior velocity. One of the earliest reported methods was introduced by Donea et al. [6]. They specified $\vec{W}$ at the next timestep by using an algebraic expression designed to calculate $\vec{W}_i^{n+1}$ as the mean of its neighboring nodes with an additional correction term included. Since then, simpler and more attractive methods have been created, one of which is the employment of a time dependent geometric transformation [20]. However, this method can only be used when the grid velocity can be found analytically.

When an analytical solution for $\vec{W}$ cannot be found, Laplacian smoothing is typically used. Laplacian smoothing involves solving the Laplacian equation, or some variation of it, over Ω such that $\vec{W}$ smoothly transitions from $\vec{U}$ to $\vec{0}$. The Laplacian equation was used by Soulaimani and Saad [24], but was later modified by Hu et al. to include a function controlling the mesh deformation [16]. The modified Laplacian equation is

$$\nabla \cdot (k_e \nabla \vec{W}) = 0, \tag{2.36}$$

where k_e is the function controlling mesh deformation [16]. The function that Hu et al. used was $k_e = A^{-1}$ where A represents the element's area (volume) in 2D (3D). By using $k_e = A^{-1}$, elements with smaller areas are forced to move rigidly while those with larger areas absorb the majority of the deformation due to the variations

in $\vec{W}$. This has the effect of preserving the quality of elements in refined regions, thus maintaining accuracy where needed. Moreover, it reduces the frequency of remeshing because larger elements can withstand more deformation than smaller elements before the element quality becomes too low.

We propose and utilize an alternate, more efficient formulation for k_e. Define a 2D element's quality, Q, as

$$Q = 4\sqrt{3}\left(\frac{A}{l_1^2 + l_2^2 + l_3^2}\right), \tag{2.37}$$

where A is the element's area and l_i is the length of side i [22]. Then the formulation for k_e is

$$k_e = (QA)^{-1} \tag{2.38}$$

and its purpose is to force low quality elements with small areas to remain rigid while forcing high quality elements with large areas to absorb the deformation from the variations in $\vec{W}$. This limits the deformation of small, low quality elements. When a remesh is determined by element quality dropping below a fixed threshold, we have found that up to 30% fewer remeshes are required when using $k_e = (QA)^{-1}$ instead of $k_e = 1$, $k_e = A^{-1}$, or $k_e = Q^{-1}$. We have also found that the error in the final solution changes minimally between simulations run with these four different versions of k_e, meaning that no version of k_e results in higher accuracy than another.

2.6 Grid Movement

To solve for $\vec{W}^{n+1}$, Equations 2.36 and 2.38 are utilized along with boundary conditions of u^{n+1} and v^{n+1}. First, Equation 2.36 is split into its component form,

multiplied by ϕ_i, and integration by parts is performed over Ω. Then the spatial discretization substitutions

$$w_u = \sum_j w_{u,h,j}\phi_j \tag{2.39}$$

and

$$w_v = \sum_j w_{v,h,j}\phi_j \tag{2.40}$$

are made, which result in a linear system of equations governing $w_{u,h}$ and $w_{v,h}$. From this point on, the subscript h will be assumed to be understood and dropped. Once w_u^{n+1} and w_v^{n+1} are found, the grid is moved utilizing

$$\left.\frac{dL}{dt}\right|_\chi = \vec{W} \approx \hat{\vec{W}}, \tag{2.41}$$

where L represents the moving grid's node locations and $\hat{\vec{W}}$ is the extrapolated approximation for $\vec{W}$. Note that L^{n+1}, and thus Ω^{n+1}, are already known when u^{n+1}, v^{n+1}, $\mathscr{P}^{n+1}$, w_u^{n+1}, and w_v^{n+1} are being found. Thus, L^{n+2} is found from Equation 2.41 and the quantities w_u^{n+1} and w_v^{n+1}. In order to stay consistent with the grid velocity reported in Equations 2.22 and 2.23 at time t^{n+2}, L^{n+2} is solved for using BDEX2. This results in

$$a_1 L^{n+2} + a_2 L^{n+1} + a_3 L^n = b\vec{W}^{n+1} + c\vec{W}^n, \tag{2.42}$$

with w_u^{n+2} and w_v^{n+2} being approximated by $\hat{w}_u^{n+2}$ and $\hat{w}_v^{n+2}$.

When using Equation 2.42 to move Taylor-Hood elements, a difficulty arises since we assume triangular elements. Let a Taylor-Hood element be exposed to the grid velocity seen in Figure 2.2a. Using Equation 2.42 to solve for all L^{n+2} points results in the element seen in Figure 2.2b. Although the grid movement has been

exaggerated for demonstrative purposes, Figure 2.2b makes it clear that a nonlinear grid velocity can distort a triangular Taylor-Hood element (dashed black line) into a non-triangular element (solid red line in Figure 2.2b). This holds true for any triangular element that utilizes nodes other than the vertex points.

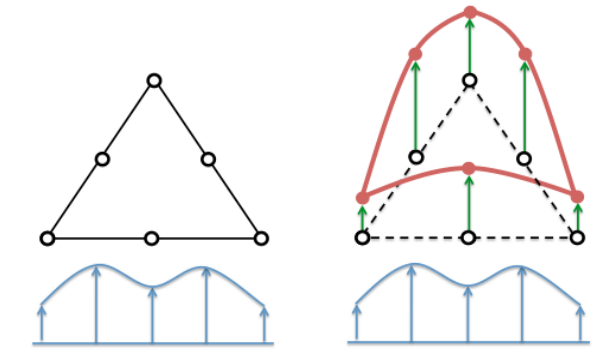

Figure 2.2: (a) Taylor-Hood nodes (hollow black points) exposed to a grid velocity (blue arrows). (b) Taylor-Hood nodes moved from original location to new location (red points) according to the grid velocity and Equation 2.42. Grid point movement is specified by green arrows.

We ensure that the elements remain triangular by implementing the following procedure. First, the vertex nodes are moved using Equation 2.42. The movement of the element's vertices is shown by the green arrows in Figure 2.3a. Next, the midpoints of the edges on the moved element are found, Figure 2.3b. Because using the grid velocity in Equation 2.42 to move the midpoints will result in a non-triangular element, the grid velocity must be adjusted to reflect the new midpoint locations. This adjusted grid velocity only applies to the midpoints and it is illustrated by the orange displacement arrows in Figure 2.3b. This method is allowable on interior points because the grid velocity is arbitrary and the process does not involve the modification of $\vec{U}$. Edge midpoints on interfaces will be artificially moved, however

no additional error is introduced when compared to using linear elements on interfaces. The adjusted grid velocity is then used in the solution of Equations 2.22, 2.23, and 2.24 at time t^{n+2}.

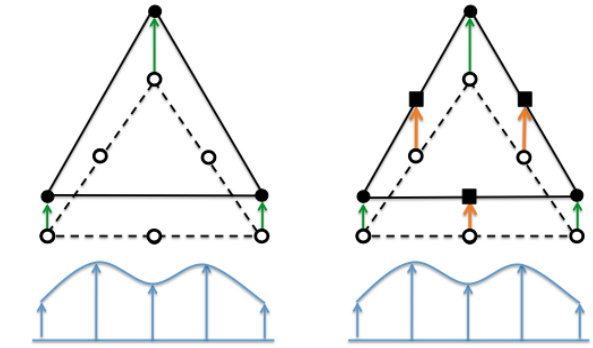

Figure 2.3: (a) Movement of the vertex points (solid black circles). Vertices' movement is specified by green arrows. (b) Placement of the edge midpoints (black squares) on the moved element. Resulting displacement of the midpoints from their original locations is shown by orange arrows.

2.7 Algorithm Overview

For each timestep, the steps of our algorithm are as follows:

1.) Check the quality of the grid. This is done locally by using Equation 2.37. Equation 2.37 will calculate the element quality such that $Q \in [0, 1]$, with 1 being the measure of an ideal element and 0 representing an undesirable element. If the quality is below a specified threshold in any location, the grid is remeshed, and the threshold can be chosen as any value between 0 and 1. However, if the threshold is fixed too high, then a significant portion of the simulation's time is spent remeshing the grid. Alternatively, if the threshold is fixed too low, then the

low quality elements cause errors to accumulate. We chose our threshold to be between 0.4 and 0.5, depending on the type of simulation. A threshold within this range avoids errors due to low quality elements, while not being too restrictive with regards to time spent remeshing. Once the grid is remeshed, or if no remesh is required, the algorithm proceeds to its next step.

2.) Find $\mathbf{\Omega^{n+1}}$. At this point in the simulation, w_u^n and w_v^n have previously been found by using Equations 2.36 and 2.38, with the known quantities u^n and v^n as boundary conditions. To find Ω^{n+1} and L^{n+1}, Equation 2.41 is solved using BDEX2 and $\vec{W}^{n+1}$ is extrapolated using the known quantities $\vec{W}^n$ and $\vec{W}^{n-1}$. Note that $\hat{\vec{W}}^{n+1}$ is modified when moving the grid's midpoint nodes (i.e. finding L^{n+1}) to ensure that the Taylor-Hood elements remain triangular.

3.) Reassemble the finite element matrices on $\mathbf{\Omega^{n+1}}$. Since the grid was moved in the second step, it is necessary to reassemble to finite element matrices over Ω^{n+1}. This is the only time that reassembly will be necessary during this timestep because the combined accuracy of the Taylor-Hood elements and BDEX2 scheme negates the need to iteratively find Ω^{n+1}.

4.) Solve Equations 2.22, 2.23, and 2.24 for $\mathbf{u^{n+1}}$, $\mathbf{v^{n+1}}$, and $\mathbf{\mathscr{P}^{n+1}}$. When solving for u^{n+1}, v^{n+1}, and $\mathscr{P}^{n+1}$, the adjusted $\hat{\vec{W}}^{n+1}$ from step 2 is used in Equations 2.22 and 2.23. This step does not require any additional measures when the stress or velocity profile on the boundaries is known a priori. However, when boundary profiles are unknown and Equations 1.1, 1.2, and 1.3 are used instead, it is necessary to divide the process of finding u^{n+1}, v^{n+1}, and $\mathscr{P}^{n+1}$ into the following substeps:

a.) First, calculate $\vec{V}^{n+1}$ and $\vec{\omega}^{n+1}$ by using $\mathscr{P}^n$ and τ_p within Equations 1.2 and 1.3. The quantity τ_p is defined as $-\mu\Big(\nabla\hat{\vec{u}}^{n+1} + (\nabla\hat{\vec{u}}^{n+1})^T\Big)$.

b.) Using $\vec{V}^{n+1}$ and $\vec{\omega}^{n+1}$ in Equation 1.1, define the velocity of the moving interfaces. Then, solve Equations 2.22, 2.23, and 2.24 for $\vec{u}^{n+1}$ and $\mathscr{P}^{n+1}$.

c.) Recalculate $\vec{V}^{n+1}$ and $\vec{\omega}^{n+1}$ by using $\mathscr{P}_c$ and τ_c within Equations 1.2 and 1.3. The quantities $\mathscr{P}_c$ and τ_c are defined as $0.5\Big(\mathscr{P}^n + \mathscr{P}^{n+1}\Big)$ and $-0.5\mu\Big[\Big(\nabla\hat{\vec{u}}^{n+1} + \nabla\vec{u}^{n+1}\Big) + \Big(\nabla\hat{\vec{u}}^{n+1} + \nabla\vec{u}^{n+1}\Big)^T\Big]$, respectively.

d.) Using $\vec{V}^{n+1}$ and $\vec{\omega}^{n+1}$ in Equation 1.1, define the velocity of the moving interfaces. Then, resolve Equations 2.22, 2.23, and 2.24 for $\vec{u}^{n+1}$ and $\mathscr{P}^{n+1}$.

e.) Repeat steps c and d until the solutions converge to within a specified tolerance. This constitutes a predictor-corrector method, PE(CE)$^\infty$, and it is important to remember that its purpose is not to iterate upon Ω^{n+1}, but $\mathscr{P}^{n+1}$, τ^{n+1}, $\vec{V}^{n+1}$, and $\vec{\omega}^{n+1}$ for the purpose of mitigating the stiffness that can arise from $(\rho_B)^{-1}$ terms.

5.) Solve Equation 2.36 for $\mathbf{w_u^{n+1}}$ and $\mathbf{w_v^{n+1}}$ using $\mathbf{u^{n+1}}$ and $\mathbf{v^{n+1}}$ as boundary conditions. At this point in time, $\hat{\vec{W}}^{n+1}$ is already known, but $\vec{W}^{n+1}$ is required for extrapolating $\vec{W}$ at the next timestep.

6.) Set $\mathbf{n+1}$ to n and repeat steps 1 through 6. Continue this process until the final simulation time has been reached.

2.8 Chapter Conclusions

The algorithm used within our ALE simulations to solve the two-dimensional, incompressible Navier-Stokes equations has been discussed. The discussion began with a translation of the conservation equations into the referential frame and a derivation of their weak formulation. The BDEX2 scheme that we use to solve the weak formulation for u^{n+1}, v^{n+1}, and $\mathscr{P}^{n+1}$ was then analyzed. Two important conclusions were made as a result of this analysis. First, when coupled with Taylor-Hood elements, the BDEX2 scheme accurately predicts Ω^{n+1} with one step. This means that iterative methods are not required when finding Ω^{n+1}, which significantly reduces the reassembly cost within our simulations compared to other ALE works. Second, it was shown that when the quantity $U_{max}\Delta x$ is less than 1.6ν, BDEX2 is guaranteed to be stable for any timestep size, which was a previously unrecognized result.

Next, the grid deformation function that we constructed was presented. Compared to other forms ($k_e = 1$, $k_e = A^{-1}$, and $k_e = Q^{-1}$), $k_e = (QA)^{-1}$ reduces the frequency of remeshing by up to 30% by forcing low quality elements with small areas to remain rigid. This rigidity and reduction of remeshing played a significant role in the success of some of the simulations that were run. In addition to discussing k_e, we addressed how triangular Taylor-Hood elements need to be moved. Finally, a detailed description of our algorithm was provided. This description included an overview of how we use the predictor-corrector method PE(CE)$^\infty$ to solve Equations 2.22, 2.23, and 2.24 when Equation 1.1 is used as a boundary condition.

In the next chapter, the algorithm, its implementation, and its capabilities are tested and validated. This is achieved through comparison to an analytical solution for the two-dimensional, incompressible Navier-Stokes equations as well as empirical approximations for drag coefficients and terminal velocities. After validation is discussed, foam bubble coarsening and the limits of the code are investigated within Chapters 4 and 5, respectively.

Chapter 3: Validation Studies

Validation of the algorithm and its implementation can be separated into two different categories. The first category of tests focuses on an analytical solution to Equations 2.7, 2.8, and 2.9 [21, 23]. The analytical solution tests are utilized not only to provide confirmation that the correct solutions for u, v, and $\mathscr{P}$ are being found, but they are also employed to study error convergence and interface tracking accuracy. Within these analytical solution tests, the boundary conditions used are a priori velocity and stress profiles. This is done so that the complex dynamics of Equations 1.2 and 1.3 do not have to be considered at this point.

Once the first category of tests is concluded, our focus turns towards these complex dynamics and validating the implementation of Equations 1.2 and 1.3. This category of tests includes investigations into the accuracy of predicted drag coefficients for stationary and moving cylinders as well as investigations into the accuracy of predicted terminal velocities for buoyant cylinders submerged in a fluid. Accuracy is determined by comparing the predicted drag coefficients and terminal velocities against empirical approximations [2, 5, 25].

3.1 Analytical Solution Validation

3.1.1 Stationary Grid Tests

The analytical solution used in the first category of tests is

$$u = 1 + 2\cos\Big(2\pi(x-t)\Big)\sin\Big(2\pi(y-t)\Big)e^{-8\pi^2\mu\rho^{-1}t}, \tag{3.1}$$

$$v = 1 - 2\sin\Big(2\pi(x-t)\Big)\cos\Big(2\pi(y-t)\Big)e^{-8\pi^2\mu\rho^{-1}t}, \tag{3.2}$$

and

$$\mathscr{P} = -\rho\Big[\cos\Big(4\pi(x-t)\Big) + \cos\Big(4\pi(y-t)\Big)\Big]e^{-16\pi^2\mu\rho^{-1}t}, \tag{3.3}$$

which is slightly modified from the equations presented in [21]. We fix $\rho = 5\,{}^{\mathrm{kg}}/_{\mathrm{m}^3}$ and $\mu = 0.5\,{}^{\mathrm{kg}}/_{\mathrm{m\cdot s}}$ to ensure a low Reynolds number flow is maintained. The tests begin with an error convergence study for several timestep and grid spacing values, Δt and Δx respectively. To ensure that Δt and Δx decrease at the same rate, the forward Euler timestep restriction is utilized during error convergence testing. Within this first error convergence study, the computational domain is a simple 1 meter by 1 meter square with Dirichlet boundary conditions on all sides. The grid is kept stationary because the grid spacing, Δx, can change arbitrarily on a moving grid.

Figure 3.1 shows the solution error plotted against the reciprocal of the grid spacing, Δx^{-1}. From Figure 3.1, it is clear that both the velocity and pressure solution behave with second order accuracy, $O(\Delta x^2)$, as indicated by the slopes of the lines. The second order accuracy is expected with regards to the velocity

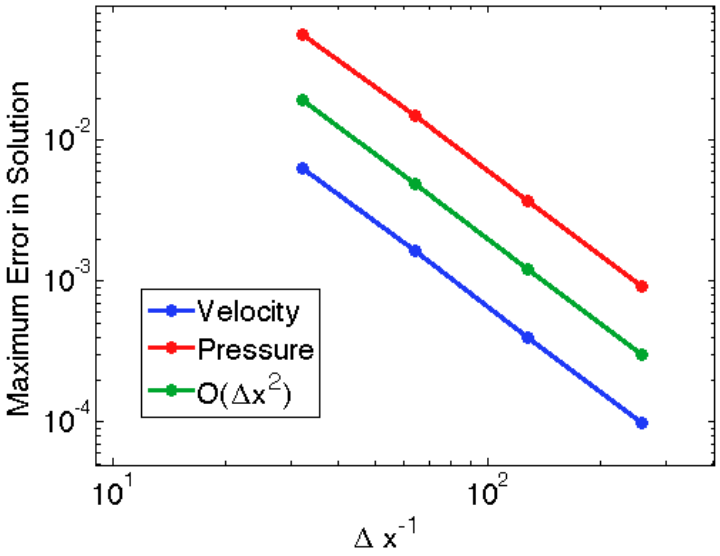

Figure 3.1: Solution error plotted against the reciprocal of the grid spacing, Δx^{-1}. Velocity and pressure errors are defined as the maximum of $||\vec{U}_{ALE} - \vec{U}||_2$ and $|\mathscr{P}_{ALE} - \mathscr{P}|$.

solution, however, the pressure solution was expected to be first order accurate due to the use of Taylor-Hood elements. We are unsure why this occurred, but having second order accuracy on $\mathscr{P}$ as well as $\vec{U}$ is certainly beneficial.

3.1.2 Moving Grid Tests

The second benchmark test within the first category consists of two parts and uses a moving mesh test similar to that proposed in [23]. First, the algorithm's ability to accurately track a moving interface is investigated. Because remeshing can affect the point distribution along an interface, the accuracy of the interface's location is investigated immediately prior to a remesh. In the second part of this test, the algorithm's error convergence is tested again, this time on a moving grid and accounting for the additional errors that arise during the remeshing process.

The same analytical solution and domain used in the first test are used in this test except a 'dyed droplet', with the same μ and ρ as the surrounding fluid, is inserted into the domain. Dirichlet boundary conditions are placed on the side walls, while the stress on the droplet's interface is specified using the analytical forms of u, v and $\mathscr{P}$ in Equations 2.13 and 2.14. A stress boundary condition is used on the droplet's interface so that the droplet is mobile and deformable without having to explicitly enforce the interfacial velocity. This allows the coupling of the interface tracking and ALE equation algorithms to be tested. The simulation's initial setup and mesh, with $\Delta x^{-1} \approx 64$, can be seen in Figure 3.2a.

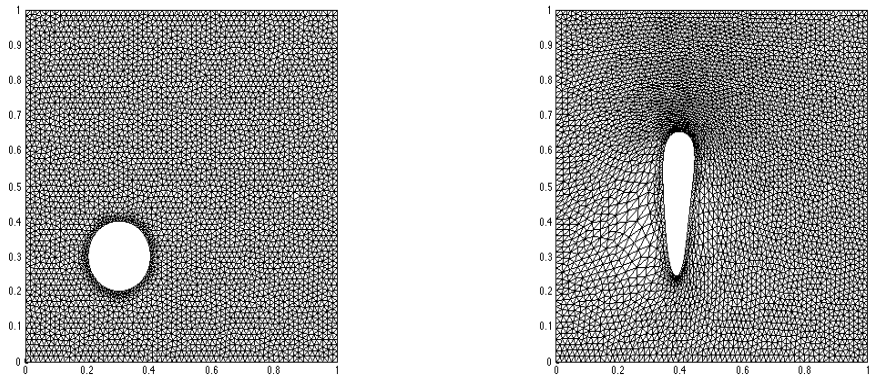

(a) (b)

Figure 3.2: Sample mesh for 'dyed droplet' error convergence test: (a) Mesh at time 0 seconds. (b) Mesh before remesh at time 0.115 seconds.

Figure 3.2b shows the deformation of the droplet and mesh before remeshing. To determine whether the predicted interface position is accurate, the analytical solutions for velocity are integrated in time using a fifth order Runge-Kutta solver. The Runge-Kutta solution for interfacial position is assumed to be exact and it is compared to the ALE-BDEX2 solution. Figure 3.3 is a plot of that comparison

corresponding to an initial grid spacing of $\Delta x^{-1} \approx 64$. Despite not employing an iterative solver to find Ω^{n+1}, one can see that the interface location is accurately captured. As expected, the error in the interface's location is proportional to the product of $||\vec{U}_{ALE} - \vec{U}||_2$ and the simulation time.

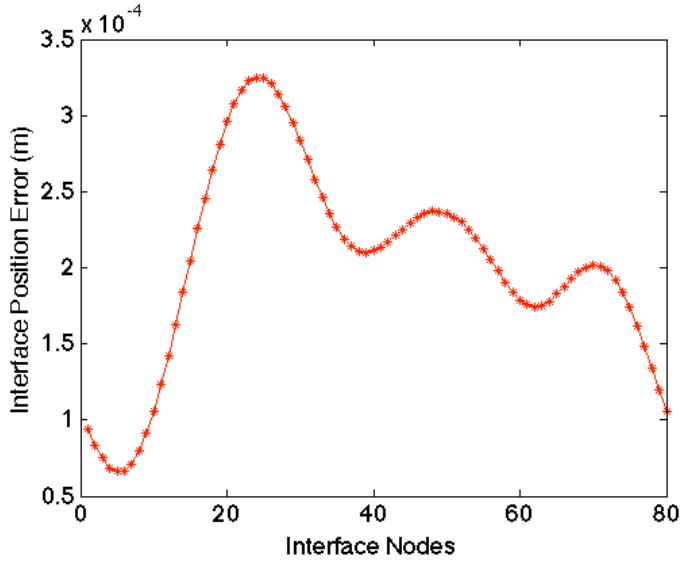

Figure 3.3: Interfacial location error for 'dyed droplet' test plotted against 80 interface nodes at time 0.115 seconds from an initial Δx^{-1} value of approximately 64. Position error is defined as $||L_{ALE} - L||_2$ with L defined from Equations 3.1 and 3.2.

After investigating the accuracy of the interface's location, the algorithm is allowed to continue, with remeshes taking place over the course of the simulation. Figures 3.4 and 3.5 are plots of $||\vec{U}_{ALE} - \vec{U}||_2$ and $|\mathscr{P}_{ALE} - \mathscr{P}|$, respectively, at the end of the simulation. At this point it needs to be mentioned that despite an initial grid density corresponding to $\Delta x^{-1} \approx 64$, very little control can be exerted upon Δx^{-1} once this ALE simulation begins. This goes for any ALE simulation and it is due to the grid deformation that takes place as well as the removal and addition of nodes that occurs during a remesh. Even with a fluid Δx^{-1}, it is clear from

Figures 3.4 and 3.5 that the errors are lower than those seen in the stationary test case for the same initial Δx^{-1}. This decrease in error is especially interesting for two reasons. First, the simulation time was decreased compared to the stationary tests. This led to a larger exponential term in the analytical solutions and it follows that this would result in larger errors. Second, and more importantly, remeshing introduces additional errors.

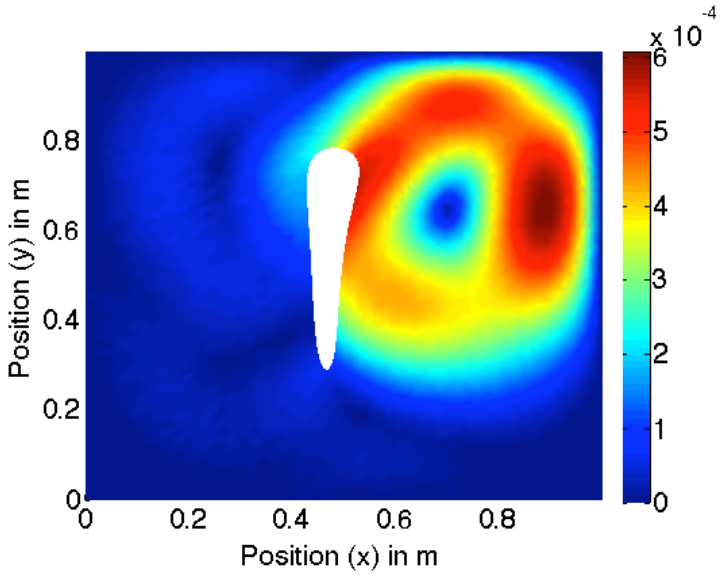

Figure 3.4: Error in solution of $\vec{U}$ at the end of the 'dyed droplet' test from an initial Δx^{-1} value of approximately 64. Error is defined as $||\vec{U}_{ALE} - \vec{U}||_2$ where $\vec{U}$ is defined by Equations 3.1 and 3.2. Regions of red signify high error and regions of blue signify little or no error.

We believe that this decrease in error is due to the mesh density near the interface. Initially, the mesh near the interface is denser than the rest of the grid, which necessitates an overall smaller timestep. Then, as the droplet deforms, regions of large curvature develop. Once a remesh is called for, the meshing routine inserts points on the surface as it sees fit. This leads to an even denser discretization near the interface and the timestep further decreases. The decreased timestep leads to a

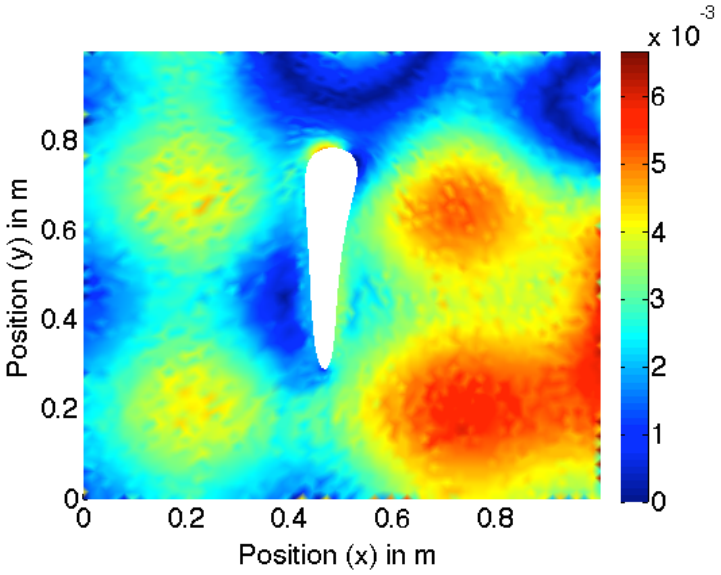

Figure 3.5: Error in solution of $\mathscr{P}$ at the end of the 'dyed droplet' test from an initial Δx^{-1} value of approximately 64. Error is defined as $|\mathscr{P}_{ALE} - \mathscr{P}|$ where $\mathscr{P}$ is defined by Equation 3.3. Regions of red signify high error and regions of blue signify little or no error.

smaller error, but this decrease in error is irrelevant if second order accuracy isn't maintained in moving grid simulations. To investigate whether $\vec{U}$ and $\mathscr{P}$ will exhibit second order accuracy again, this test is repeated for two other values of Δx^{-1}.

Figure 3.6 is a plot of the error convergence for this test. Note that the error results are plotted against the initial values of Δx^{-1}. The values of Δx change over the course of the simulations, but the majority of nodes maintain a spacing approximately equal to the initial Δx spacing. By comparing Figure 3.6 to Figure 3.1, two things become immediately apparent. First, all of the errors in Figure 3.6 are smaller than their counterparts in Figure 3.1. Again, we believe that this is due to the increase in grid density in the vicinity of the interface. Second, the order of accuracy observed in Figure 3.1 is also present in Figure 3.6 despite the additional errors that are introduced in moving grid simulations.

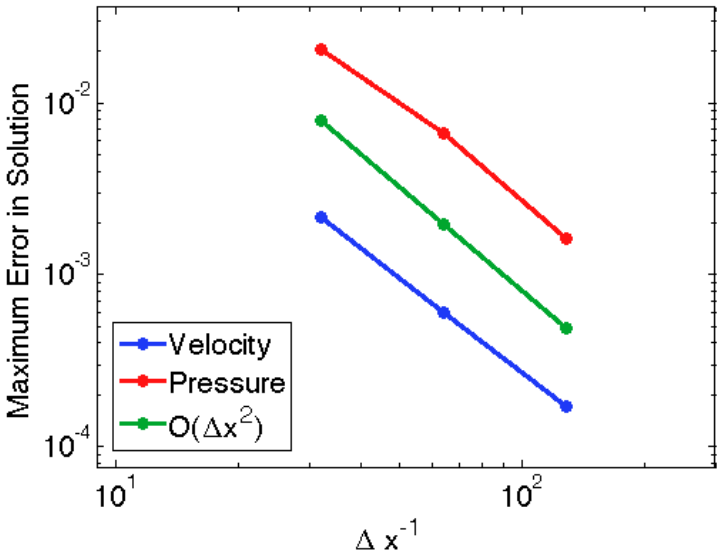

Figure 3.6: ALE solution error plotted against the reciprocal of the initial grid spacing, Δx^{-1}. Velocity and pressure errors are defined as the maximum of $||\vec{U}_{ALE} - \vec{U}||_2$ and $|\mathscr{P}_{ALE} - \mathscr{P}|$ where $\vec{U}$ and $\mathscr{P}$ are defined by Equations 3.1, 3.2, and 3.3.

3.2 Buoyant Cylinder Validation

3.2.1 Free Stream Flow Tests

As was previously mentioned, the models we are interested in building require the ability to accurately resolve flow fields and the capability to handle free body motion. After validating our ability to accurately resolve flow fields, our attention turns towards investigating the complex dynamics that Equations 1.2 and 1.3 introduce when Equation 1.1 is used as a boundary condition. To simplify the process, the surface stress forces of Equations 1.2 and 1.3 are investigated first through a drag coefficient study. Then, both the surface stress buoyancy forces are considered in the final validation stage. All tests consider a cylinder placed along a fluid filled

container's centerline.

We begin our drag coefficient studies by exposing a 2D cylinder, of radius 10^{-4}m, to an infinite, free stream flow, which has a unidirectional velocity of $(0, V_\infty)$. The drag coefficient, C_D, is governed by

$$C_D = \frac{F_D}{\rho V_\infty^2 r_B} \tag{3.4}$$

with the drag force, F_D, defined as

$$F_D = -\int_\Gamma (\mathscr{P}\vec{n} + \tau \cdot \vec{n})\, d\Gamma. \tag{3.5}$$

There are several analytical expressions and empirical data sets for C_D at steady state as a function of Reynolds number. Within this study, we compare our results to the empirical data published in [5]. To mimic the infinite, free stream flow studied by Dennis et al., the model considers a container wide and tall enough such that the boundary effects are minimized. The container walls are given Dirichlet boundary conditions of $(0, V_\infty)$ and the fluid inside of the channel is taken to be water, with $\rho = 10^3\ {}^{\mathrm{kg}}/_{\mathrm{m}^3}$ and $\mu = 10^{-3}\ {}^{\mathrm{kg}}/_{(\mathrm{m}\cdot\mathrm{s})}$.

Within the model, different values of C_D are explored by varying the magnitude of V_∞. This allows us to compare our results to those of Dennis et al. for several representative values of Re. Figure 3.7 shows the results of this comparison. From Figure 3.7, it is clear that there is excellent agreement between our results and the values presented in [5]. In fact, we are able to reproduce Dennis et al.'s results for Re values well outside of the range we would expect to encounter within liquid channels of micro-foams and micro-emulsions. This is an encouraging result, but C_D

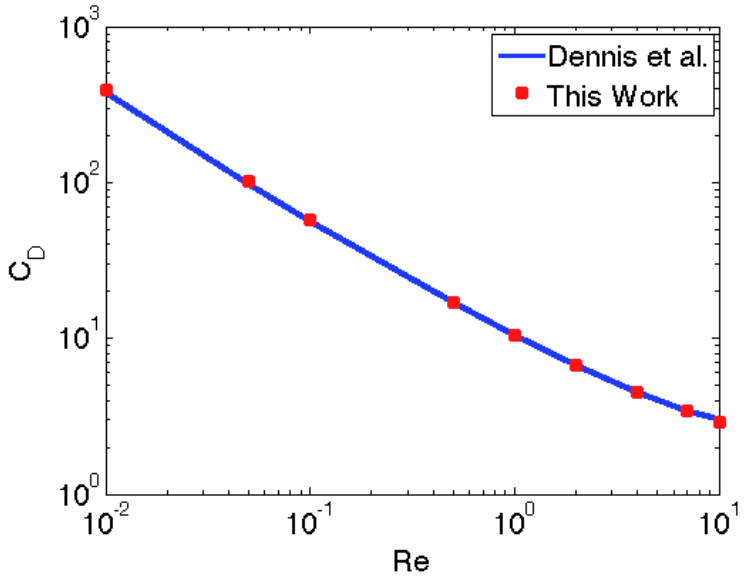

Figure 3.7: Comparison of the drag coefficients of a stationary cylinder in free stream flows as a function of Reynolds number against the work of [5].

is comprised of two components, the viscous drag coefficient (C_F) and the pressure drag coefficient (C_P). The viscous drag coefficient, C_F, is governed by

$$C_F = \frac{F_\mu}{\rho V_\infty^2 r_B} \tag{3.6}$$

with the viscous drag force, F_μ, defined as

$$F_\mu = -\int_\Gamma \tau \cdot \vec{n}\, d\Gamma \tag{3.7}$$

and the pressure drag coefficient, C_P, is governed by

$$C_P = \frac{F_P}{\rho V_\infty^2 r_B} \tag{3.8}$$

with the pressure drag force, F_P, defined as

$$F_P = -\int_\Gamma \mathscr{P}\vec{n}\, d\Gamma. \tag{3.9}$$

Can C_F and C_P be captured with the same accuracy as C_D? To answer that, we repeat the drag coefficient study, monitoring C_F and C_P rather than C_D, and compare the results to the values published in [5].

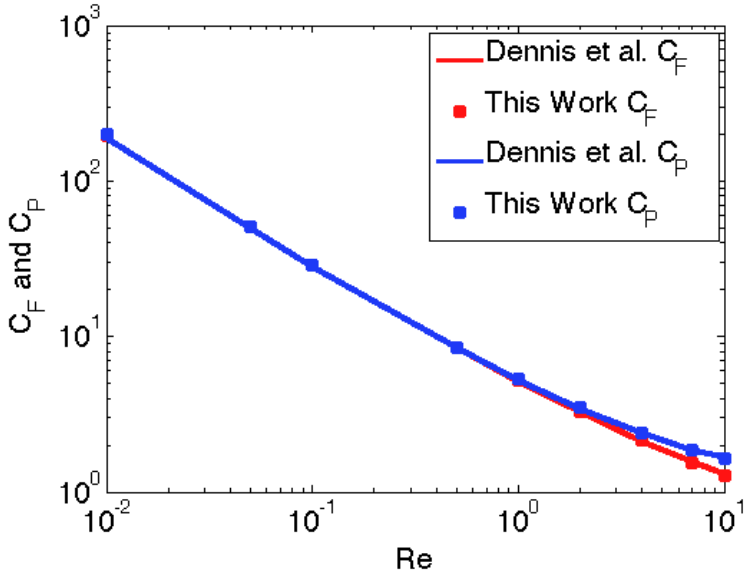

Figure 3.8: Comparison of the viscous and pressure drag coefficients of a stationary cylinder in free stream flows as a function of Reynolds number against the work of [5].

Figure 3.8 shows the results of this comparison. From Figure 3.8, excellent agreement between our results and the values from [5] can be seen. In fact, C_F and C_P were captured with the same accuracy as C_D. Most importantly, the divergence of C_F and C_P that takes place at $Re > 1$ was reproduced. With these results, we consider our free stream drag coefficient tests complete and we move towards incorporating wall effects into these calculations.

3.2.2 Wall Effects Tests

When walls are in the near vicinity of an object, their presence can add significant drag to the surface of the object. To understand why this occurs, consider a fluid filled channel with a cylinder placed inside. As the fluid approaches and passes the cylinder, the fluid must accelerate in the area between the side walls and cylinder in order to conserve mass. This accelerated fluid velocity causes the cylinder's surface to experience increased stresses compared to the stresses that the incoming velocity would cause. If the side walls are moved closer to the cylinder, the surface stresses will increase because the passing fluid would have to undergo a larger acceleration. Similarly, if the side walls are moved away from the cylinder, the surface stresses will decrease until the walls reach a distance at which the cylinder cannot feel their effects. Thus, C_D is a function of Re and ξ, the ratio of the channel width to droplet diameter.

The effects of walls, and neighboring objects, will play an important role within our micro-foam and micro-emulsion studies. Therefore, it is critical to validate the additional stresses within the model. The validation process consists of two separate types of simulations involving a cylinder within a water filled container. The first type considers the position of the cylinder to be fixed and the fluid is specified to enter and exit the container with a fixed velocity of $(0, V_\infty)$. The second type considers the cylinder moving at a fixed velocity of $(0, V_\infty)$ within a closed container. For both cases, the position of the cylinder is such that the top and bottom boundaries do not affect the drag forces experienced by the cylinder's surface. In addition, Re and

V_∞ are fixed within these simulations and ξ is varied so that different values of C_D can be explored. Theoretically, there should exist no differences in C_D between the moving cylinder and stationary cylinder simulation results. However, it is important to test and confirm this in order to validate the moving body simulations.

There are several steady state analytical expressions and empirical data sets for C_D within the literature that take wall effects into account. The two sources that will be used for comparison within this work are [25] and [2]. Takaisi presented an analytical expression for C_D as a function of Reynolds number and ξ, but it is only valid for small Reynolds numbers and large values of ξ. This is due to the Stokes flow assumption that Takaisi employed. Within [2], numerical and experimental data points are presented for C_D as a function of ξ. However, these numerical and experimental results diverge when ξ decreases below 2. For this reason, values of $\xi < 2$ will not be considered here.

Figure 3.9 contains the comparison between Takaisi's analytical approximation, Bouard et al.'s numerical data, and the results from both the stationary and moving cylinder simulations. First and foremost, we can see from Figure 3.9 that the stationary and moving cylinder results are in total agreement, as expected. As for the comparison with published data, it is clear that there is a good consensus between the results of this work and Takaisi's analytical expression for the values of ξ when the Stokes flow assumption is valid. Once Takaisi's expression becomes invalid, for $\xi < 4$, comparisons must continue against the results of [2]. From Figure 3.9, we can see that the consensus between our results and those of Bouard et al. is excellent for all values of ξ. The results from this test, as well as the free stream test

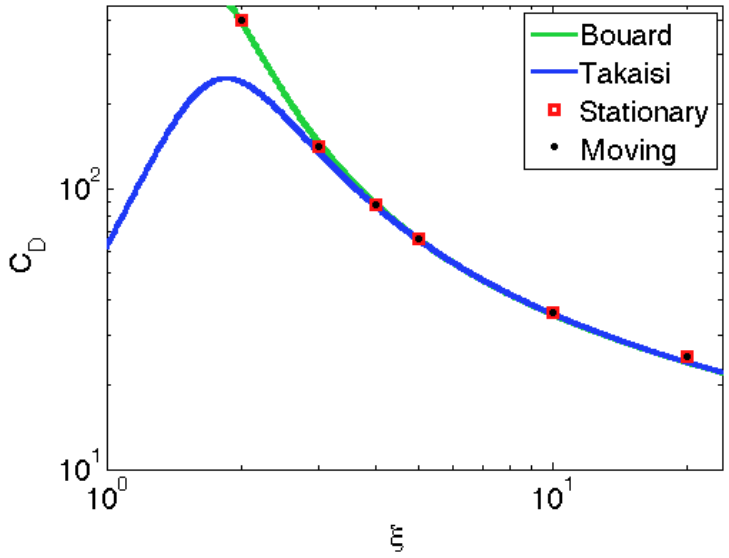

Figure 3.9: Comparison of the drag coefficient of a stationary cylinder and a moving cylinder as a function of ξ against the works of [2, 25].

results, give us total confidence in the algorithm's ability to calculate the surface stresses.

3.2.3 Terminal Velocity Tests

With confidence in the surface stresses, the focus of validation turns towards the terminal velocity, V_T, of a buoyant cylinder. For these tests, a buoyant cylinder is placed inside a container with no-slip conditions on all four walls. The height of the container and position of the cylinder are such that the top and bottom of the container do not effect the motion of the droplet. The results from this model at steady state will be compared to

$$V_T = \left[\ln(\xi) - 0.9156 + 1.7243\xi^{-2}\right]\left(\frac{r_B^2(\rho - \rho_B)g_y}{4\mu}\right) \tag{3.10}$$

where g_y is the vertical component of $\vec{g}$. This expression for V_T can be derived by balancing Takaisi's expression for F_D with the buoyancy force. The model takes ρ and ρ_B to be fixed at $10^3\,{}^{\mathrm{kg}}/_{\mathrm{m}^3}$ and $930\,{}^{\mathrm{kg}}/_{\mathrm{m}^3}$, respectively, and several values of V_T are explored by varying μ. It is important to remember that inherent to Equation 3.10 is the Stokes flow assumption. This means that Equation 3.10 can only be used to calculate V_T when $\xi \geq 4$ and Re remains small. Thus, the container width is set such that $\xi = 10$ and μ is kept in a range such that $Re \leq 0.5$.

The results of this testing can be seen in Figure 3.10. Figure 3.10 shows that the numerical results match with the analytical approximation, Equation 3.10. In fact, the differences are less than 2%. Smaller differences could have been achieved by letting the simulations run for a longer period of time, however, they would have been extremely expensive. With these results, as well as our drag coefficient testing results, we can conclude our free body problem validation testing.

3.3 Chapter Conclusions

Within this chapter, we have validated our algorithm and its implementation. Two types of studies were considered during this validation. The first consisted of comparing an analytical solution for u, v, and $\mathscr{P}$ to our code's results for stationary and moving grids. For both types of grids, error convergence tests were performed and second order accuracy was evidenced each time. The moving grid test also included an investigation into interface tracking accuracy. It was shown that the BDEX2 algorithm is capable of accurately tracking an interface, despite

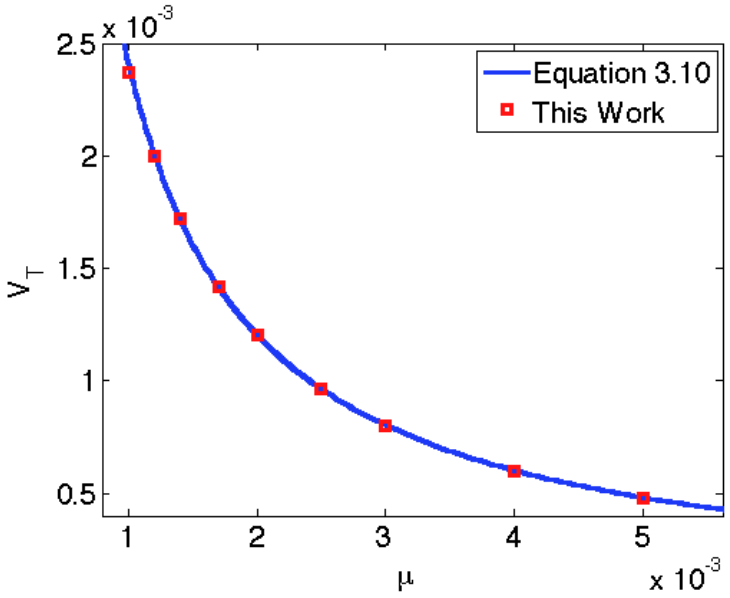

Figure 3.10: Comparison of the terminal velocities of a cylinder as a function of μ against Equation 3.10.

not employing iterative methods to find Ω^{n+1}.

The second type of study focused on the free body problem by testing predicted drag coefficients and terminal velocities. Since Equations 1.2 and 1.3 introduce complex dynamics through the boundary condition Equation 1.1, it was important to validate each aspect of Equations 1.2 and 1.3. Testing began with drag coefficient studies in free stream flows to ensure that the surface stresses were being accurately calculated. Agreement between our drag coefficients and those from [5] were excellent. Drag coefficient testing continued by moving the walls of the container inwards such that the wall effects could be studied. An analytical expression for C_D from [25] and numerical results for C_D from [2] were used for comparison. Our results were again in excellent agreement with the published results. Finally, the terminal velocities of a buoyant cylinder were investigated and we compared our

results to a derived approximation for V_T, Equation 3.10. The differences between our numerical results and Equation 3.10 were less than 2%.

The results from this series of tests validate our algorithm and its implementation. In the next chapter, foam coarsening is investigated on the local scale. Within the literature, there exist multiple, global studies on coarsening. However, questions can be raised regarding the assumptions that these global studies make. These questions suggest that there remain some fundamental misunderstandings about the coarsening process. In an attempt to gain a better understanding, we create a local model of coarsening. After coarsening is investigated, the capabilities of the algorithm are thoroughly tested.

Chapter 4: Foam Coarsening

Coarsening is a well recognized phenomenon that takes place in aging foams. It is the process by which a foam's average bubble size increases over time (see Figure 4.1). Theory attributes this increase in average bubble size to the diffusion of gas from small bubbles to large bubbles. Since coarsening depends on the rate at which dissolved gas diffuses through the liquid phase, the timescales for coarsening can be larger than those of drainage. However, there are situations where drainage does not occur until coarsening takes place. An example of this is drainage in shaving cream.

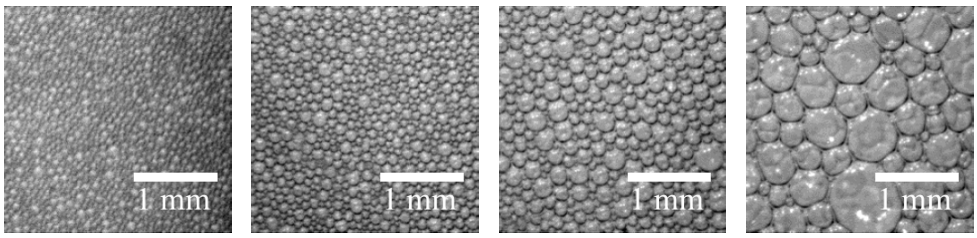

Figure 4.1: Time series depiction of a coarsening foam from experiments conducted by Kennedy et al.: (a) 30 seconds, (b) 100 seconds, (c) 300 seconds, (d) 1000 seconds.

There are multiple works within the current literature where the coupling of drainage and coarsening is investigated [13, 17, 26]. These works have utilized global

continuum models to study coarsening and have explained the rate at which a foam's average bubble size grows over time in a satisfactory manner. However, within these models, the foam's bubbles are assumed to be mono-disperse. In addition, the film thicknesses, defined as the distances between bubbles across which gas diffuses, are assumed to be constant.

From a physical perspective, questions can be raised about the relevance of these assumptions. First and foremost, if all of the bubbles within a foam were mono-disperse, coarsening would not take place. This is because bubble size differences cause gas solubility gradients in the liquid adjacent to the bubbles. These solubility gradients drive the exchange of gas between bubbles, which causes coarsening. Second, it is not unreasonable to expect the film thicknesses to change as the bubbles themselves change over time. Changes in film thicknesses would affect the diffusion of gas, which would directly affect how bubbles coarsen.

Even with the success of previous models, the questions about their assumptions suggest that there remain some fundamental misunderstandings with regards to coarsening. In hopes of gaining a better understanding, we study coarsening locally. Specifically, we want to investigate the effects of changing film thicknesses on foam coarsening and drainage, without assuming mono-disperse bubbles.

We investigate these effects by studying an idealized, poly-disperse foam with our 2D incompressible, Navier-Stokes ALE model. Within our model, we allow the bubbles to coarsen according to their size and film thicknesses and we assume that the gravity and capillarity forces are balanced at all times. Without considering coarsening, the assumption of balanced gravity and capillarity forces would result

in the foam not draining. However, that is not to say that this assumption is unreasonable (e.g. shaving cream). Coarsening, and the interstitial fluid flow it causes, is captured in the model by relating the velocity of each bubble's interface with an expression governing the rate of coarsening for that bubble.

Our 2D incompressible, Navier-Stokes ALE model is perfectly suited for this problem since our ALE model is capable of accurately tracking the moving bubble interfaces while resolving the interstitial flow fields caused by the bubble's interfacial movement. Our model's capabilities enable us to study this highly nonlinear coupling of coarsening and fluid flow and we compare our model's results to the experimental drainage data from [17] in order to determine the effects of changing film thicknesses. This comparison is made by calculating our foam's drainage velocity as the interstitial fluid's average vertical velocity along a horizontal cross section of the domain.

4.1 The Drainage Model

Our idealized foam is comprised of three bubbles that remain circular for all times. This idealized foam is not meant to simulate a real foam per se, but rather its purpose is to give us the ability to qualitatively understand the physics governing the individual bubble sizes and the local liquid drainage. After the local physics are understood, the model can be made more comprehensive through geometric scaling and by including additional phenomena.

The bubble's radii are chosen such that our foam is poly-disperse and the

bubbles are on the same scale as the bubbles observed by Kennedy et al.. The bubbles are stacked one on top of another within a rectangular container. The largest bubble is placed on top of the stack, the smallest bubble on the bottom of the stack, and the three centers are fixed. The distances between the bubble interfaces are initially specified to be equal, however, they are chosen with the simulation's run time and the bubble's circularity in mind. As is explained later in this work, the distances themselves are almost immaterial because of how the coarsening equations take film thicknesses into account. However, the distances chosen still correspond to values one could expect to find in an actual foam.

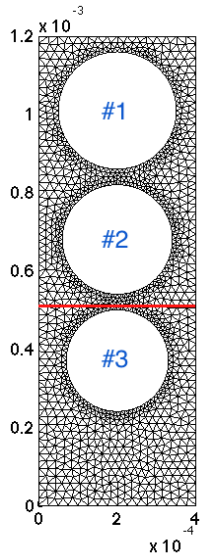

Figure 4.2: Depiction of the idealized foam with the rectangular container. The red line represents the line along which the drainage velocity is calculated.

Figure 4.2 depicts the idealized foam and its setup, as well as the line across which the foam's drainage velocity is calculated. Drainage is not calculated at the bottom of our foam because we enforce conservation of mass upon the system. No slip boundary conditions are placed on the top and sides of the container. Even

with mass being conserved, it is necessary to place a no stress boundary condition on the bottom of the container due to the effects that numerical round off errors have on the incompressibility restraint. The bottom of the container is placed far enough away such that the no stress condition does not affect the drainage results.

We allow our poly-disperse foam to coarsen by tracking the flux of gas that occurs between different sized bubbles. As the bubbles grow (shrink), the bubbles push (pull) upon the surrounding interstitial fluid, which causes local fluid flow. We specify the velocity of the interstitial fluid immediately surrounding the bubbles by implementing Dirichlet boundary conditions of

$$u_i = \cos(\theta_i)\left(\frac{dR_i}{dt}\right) \tag{4.1}$$

and

$$v_i = \sin(\theta_i)\left(\frac{dR_i}{dt}\right) \tag{4.2}$$

on Bubble i's surface. Within Equations 4.1 and 4.2, θ_i is a vector of the polar angles formed by all of the boundary nodes on Bubble i, u_i is the horizontal velocity of those boundary nodes, v_i is the vertical velocity of those boundary nodes, R_i is the radius of Bubble i, and $\frac{dR_i}{dt}$ is the rate of coarsening for Bubble i.

The velocities u_i and v_i are not known a priori, but they are specified during the simulation according to our coarsening equations and the θ_i values. Our coarsening equations govern $\frac{dR_i}{dt}$ for each bubble and they are derived such that the local, diffusive transport of gas between bubbles (according to their differences in size) is taken into account. The benefits of treating coarsening and the bubble interfaces in this fashion are twofold. First, the equations for $\frac{dR_i}{dt}$ and their use in Equations

4.1 and 4.2 allow us to couple coarsening to drainage. Without coarsening in our model, drainage would not occur, which makes this coupling an important physical mechanism in our simulations. Second, these equations enable us to investigate the effects of changing film thicknesses and constant film thicknesses on coarsening, and thus drainage.

It is this ability to accommodate changing film thicknesses within our coarsening equations that forms the crux of our study. Yet, it isn't obvious how these rates of coarsening should be specified on the local scale. Within global coarsening works, see [26], the accepted coarsening equation is

$$\frac{dR}{dt} = D\frac{F(\kappa)}{R} \tag{4.3}$$

where D is a constant, effective diffusion coefficient for the dissolved gas in the liquid phase, R is the foam's average bubble radius, and $F(\kappa)$ is a function that relates the rate of coarsening to the foam's liquid fraction, κ. Please see Appendix A for how D is defined within [17]. Typically, the dry foam limit, $F(\kappa) = 1$, is assumed within coarsening studies [17]. Despite their wide acceptance, the dry foam limit and Equation 4.3 only allow coarsening to be captured on the global scale. They are not applicable on the local scale.

For the local scale, as was mentioned previously, separate equations must be derived for each bubble and the differences between the bubble's interior pressures must be taken into account. The derivation of the two sets of equations we use to specify R_1, R_2, and R_3 as functions of time can be seen in Appendix A. The first

set of equations considers constant film thicknesses and is represented by

$$\frac{dR_1}{dt} = D\left(\frac{\sin^{-1}\left(\frac{R_2}{R_1}\right)}{\pi}\right)\left(\frac{1}{R_2} - \frac{1}{R_1}\right), \tag{4.4}$$

$$\frac{dR_2}{dt} = -\frac{R_1}{R_2}\frac{dR_1}{dt} - \frac{R_3}{R_2}\frac{dR_3}{dt}, \tag{4.5}$$

and

$$\frac{dR_3}{dt} = D\left(\frac{\sin^{-1}\left(\frac{R_3}{R_2}\right)}{\pi}\right)\left(\frac{1}{R_3} - \frac{R_2}{R_3^2}\right). \tag{4.6}$$

The second set of equations considers varying film thicknesses and is represented by

$$\frac{dR_1}{dt} = \left(\frac{D\lambda_a^0}{\lambda_a}\right)\left(\frac{\sin^{-1}\left(\frac{R_2}{R_1}\right)}{\pi}\right)\left(\frac{1}{R_2} - \frac{1}{R_1}\right), \tag{4.7}$$

$$\frac{dR_2}{dt} = -\frac{R_1}{R_2}\frac{dR_1}{dt} - \frac{R_3}{R_2}\frac{dR_3}{dt}, \tag{4.8}$$

and

$$\frac{dR_3}{dt} = \left(\frac{D\lambda_b^0}{\lambda_b}\right)\left(\frac{\sin^{-1}\left(\frac{R_3}{R_2}\right)}{\pi}\right)\left(\frac{1}{R_3} - \frac{R_2}{R_3^2}\right). \tag{4.9}$$

Figure 4.3 shows the changes in bubble sizes when Equations 4.4, 4.5, and 4.6 are used and Figure 4.4 shows the changes in bubble sizes when Equations 4.7, 4.8, and 4.9 are used. From Figures 4.3 and 4.4, qualitative differences between the resulting bubbles can easily be seen. Simply put, Equations 4.4, 4.5, and 4.6 cause two large bubbles and one small bubble to develop over the course of 200 seconds. On the other hand, one large bubble and two smaller bubbles develop by the end of 200 seconds when Equations 4.7, 4.8, and 4.9 are used.

Local dynamics of this type cannot be captured with a global model. However, it isn't obvious which set of coarsening equations better represents the local

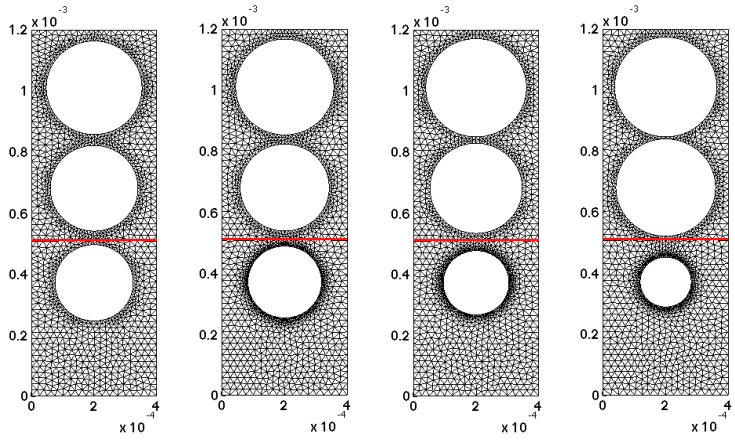

(a) (b) (c) (d)

Figure 4.3: Time series depiction of the foam when constant film thicknesses are assumed: (a) 50 seconds, (b) 100 seconds, (c) 150 seconds, (d) 200 seconds. For reference, we include the line across which the drainage velocity is calculated.

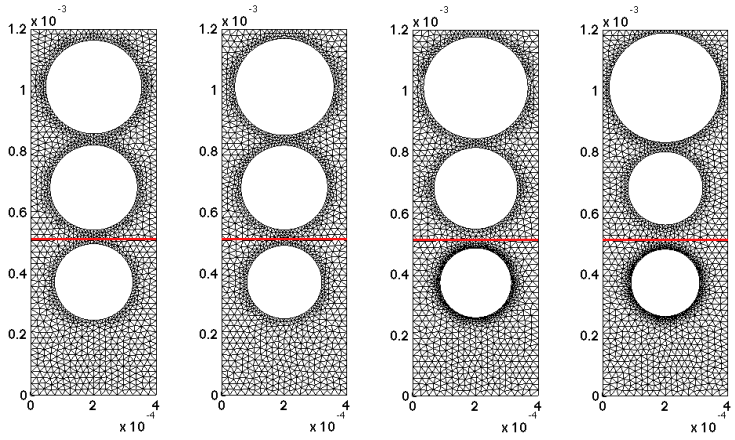

(a) (b) (c) (d)

Figure 4.4: Time series depiction of the foam when varying film thicknesses are allowed: (a) 50 seconds, (b) 100 seconds, (c) 150 seconds, (d) 200 seconds. For reference, we include the line across which the drainage velocity is calculated.

dynamics that were observed in the experiments of Kennedy et al. Based on how coarsening is coupled to the foam's interstitial fluid within our model, the differences between the two sets of coarsening equations will manifest themselves in the calculated drainage velocities. To determine which set of equations is more representative

of what occurs on the local scale during coarsening, the drainage profiles that each set of coarsening equations causes is compared to experimental data from [17].

4.2 Drainage Velocity Comparison

To determine which set of equations best describes coarsening on a local scale, we compare the drainage that results from using Equations 4.4, 4.5, and 4.6 in Equations 4.1 and 4.2 and the drainage that results from using Equations 4.7, 4.8, and 4.9 in Equations 4.1 and 4.2 against drainage data published by [17]. The drainage data published by Kennedy et al. is in the form of grams versus time. We translate the data from grams versus time to velocity versus time by taking the time derivative of the drained liquid's measured height, H.

Due to the nature of the experiment's data collection, the time derivative data is extremely noisy. To mollify the noise, the time derivative of H is approximated by using centered differencing at representative data points with timesteps much larger than the data collection frequency. The results of this approximation are represented by the black line in Figure 4.5. It is clear from Figure 4.5 that some noise still remains in the drainage velocity approximation. To remove this remaining noise, arithmetic mean filtering is used and the results of this smoothing are represented by the red line shown in Figure 4.5.

When Equations 4.4, 4.5, and 4.6 are used within Equations 4.1 and 4.2, the fluid flow they cause at 200 seconds can be seen in Figure 4.6a. Similarly, the fluid flow at 200 seconds that Equations 4.7, 4.8, and 4.9 cause when used within

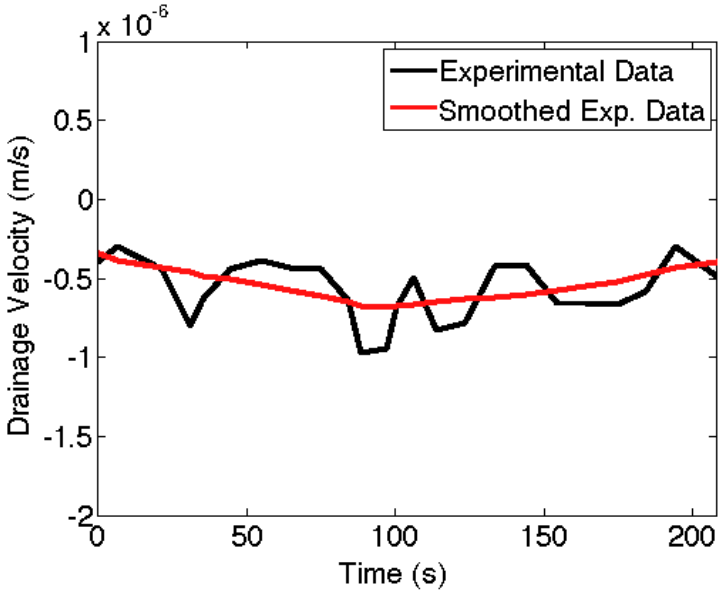

Figure 4.5: Experimental drainage velocity [17]. The velocity derived from changes in H is seen with the black line. The smoothed velocity is seen with the red line.

Equations 4.1 and 4.2 can be seen in Figure 4.6b. By averaging the vertical velocity of the interstitial fluid for all times along the (red) cross section in Figures 4.6a and 4.6b, Figure 4.7 is created. Within Figure 4.7, the green line represents the drainage caused by Equations 4.4, 4.5, and 4.6 and the blue line represents the drainage caused by Equations 4.7, 4.8, and 4.9. In addition, Figure 4.7 contains the smoothed drainage velocity data from Kennedy et al..

There are several factors within our model that will not allow us to make quantitative comparisons to experimental data. For example, the specific values of V_m, D_f, He, and γ that we chose, along with the dimensions of our initial setup, could alter the drainage velocity that we experienced. More importantly, our model is 2D and the data from Kennedy et al. is 3D. Yet, important conclusions can be drawn from the qualitative aspects of Figure 4.7. Namely, the drainage caused by

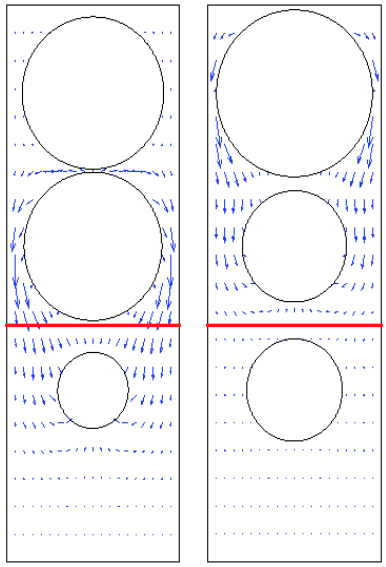

(a) (b)

Figure 4.6: Interstitial flow field at 200 seconds caused (a) when constant film thicknesses are assumed (b) when varying film thicknesses are allowed.

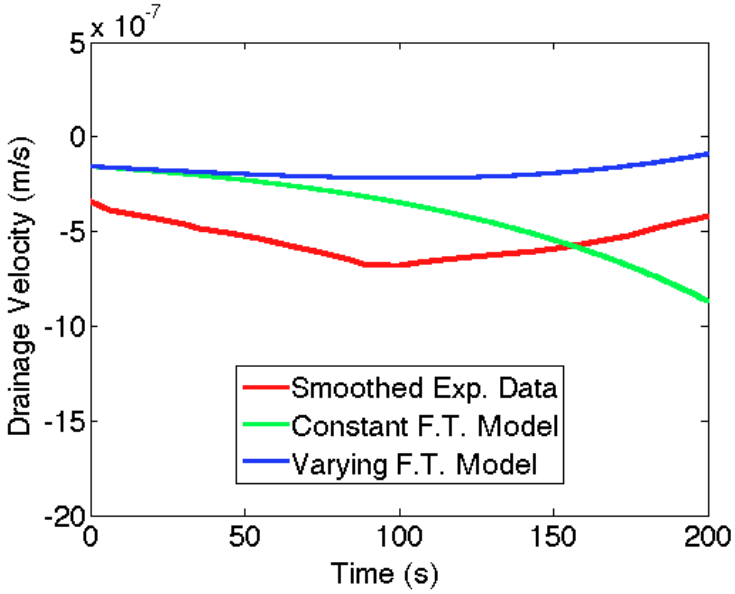

Figure 4.7: Drainage velocities produced by our ALE models with the smoothed experimental data from Kennedy et al. (red) included for reference. The constant film thicknesses (F.T.) model produced the velocity depicted by the green line and the varying film thicknesses model produced the blue line.

Equations 4.7, 4.8, and 4.9 is almost identical in nature to the experimental data. Both curves exhibit a period of acceleration in drainage velocity as well as a period of deceleration. In fact, the timescales and magnitudes of this acceleration and deceleration are comparable between the curves. The drainage caused by Equations 4.4, 4.5, and 4.6 accelerates over the entire time period and its curve does not mimic the experimental data. Thus, it is clear that coarsening is best captured on the local scale when film thicknesses are allowed to vary within the model.

4.3 Bubble Size Study

With the comparison between the model results and experimental data suggesting that changing film thicknesses better represent the local dynamics of coarsening and drainage, we looked back at Figure 4.4, specifically Figure 4.4d. Originally, Bubble 2 was larger than Bubble 3, but Figure 4.4 shows the shrinking of Bubble 2, with Bubbles 2 and 3 appearing to be equal in size in Figure 4.4d. This is in direct contrast to the dynamics that Equations 4.4, 4.5, and 4.6 enforce, as seen in Figure 4.3.

Current coarsening theory says that larger bubbles grow at the expense of smaller bubbles. However, with Bubble 2 approaching the size of Bubble 3, is it possible for Bubble 2 to become smaller than Bubble 3? This would cause the flux of gas from Bubble 3 to Bubble 2 to change direction and gas would instead flux from Bubble 2 to Bubble 3. To investigate whether this switch in size will occur, we solve Equations 4.7, 4.8, and 4.9 for R_1, R_2, and R_3 over the course of 300 seconds,

without taking drainage into account.

There are two side effects of modeling beyond the 200 seconds considered in the drainage study; one of which is expected. First, Bubble 1 outgrows the original container over the course of 300 seconds. Thus, the original container can not be used here. Second, Bubble 2 does indeed become smaller than Bubble 3. This switch of $R_2 > R_3$ to $R_3 > R_2$ causes the direction of the gas flux to change and invalidates Equation 4.9. It becomes necessary to replace Equation 4.9 with

$$\frac{dR_3}{dt} = \left(\frac{D\lambda_b^0}{\lambda_b}\right)\left(\frac{\sin^{-1}\left(\frac{R_2}{R_3}\right)}{\pi}\right)\left(\frac{1}{R_2} - \frac{1}{R_3}\right). \tag{4.10}$$

Equation 4.10 can be derived by simply replacing the view factor within Equation 4.9 with a view factor that reflects the transfer of gas from Bubble 2 to Bubble 3.

Figure 4.8 contains a plot of R_1, R_2, and R_3 when Equations 4.7, 4.8, 4.9, and 4.10 are used. From Figure 4.8, it can be seen that despite R_2 initially being larger than R_3, Bubbles 2 and 3 become identical in size at approximately 225 seconds. After that point in time, R_2 continues to decrease until Bubble 2 disappears completely (not shown). At the same time, Bubble 3 increases in size slightly, which can be explained by the transport of gas from Bubble 2 to Bubble 3. In order to put the results of Figure 4.8 into perspective, Figure 4.9 contains snapshots of the bubbles in a fashion similar to that of Figures 4.3 and 4.4.

Although the disappearance of Bubble 2 before Bubble 3, as foreshadowed by Figures 4.8 and 4.9, is surprising with respect to current coarsening theory, the dynamics of Bubble 2 can be explained by considering the film thicknesses, λ_a and λ_b. Figure 4.10 shows λ_a and λ_b over time. The gap between Bubbles 1 and 2 and

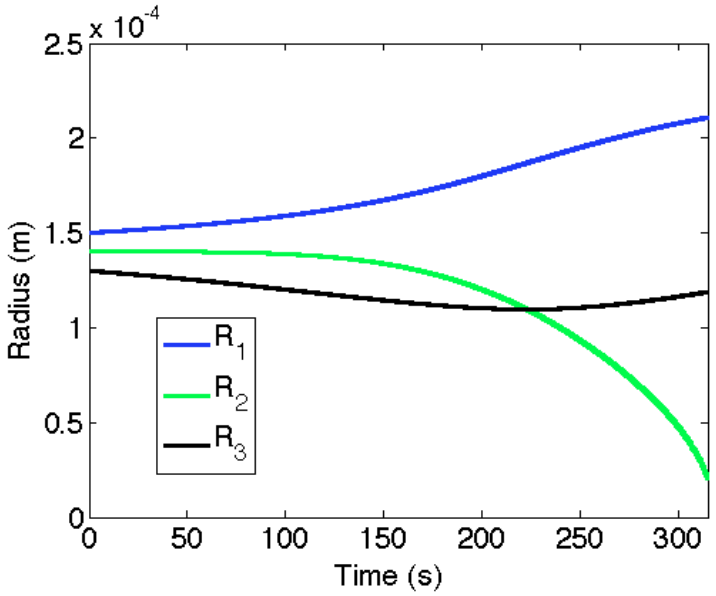

Figure 4.8: Radii over the course of 300 seconds when varying film thicknesses are allowed.

the gap between Bubbles 2 and 3 are initially the same, but they soon diverge. The quantity λ_a quickly becomes smaller than λ_b, meaning that the rate of gas diffusion from Bubble 2 to Bubble 1 is faster than that from Bubble 3 to Bubble 2. Bubble 2 begins to shrink, as evidenced around 100 seconds in Figure 4.8, due to the gas supply deficit. To the benefit of Bubble 1, Bubble 2 continues to shrink until it and Bubble 3 are the same size. After 225 seconds, Bubbles 1 and 3 grow at the expense of Bubble 2, which quickly causes Bubble 2's gas supply to become exhausted.

4.4 Chapter Conclusions

We have constructed an idealized foam for the purpose of studying local coarsening and drainage with our ALE model. The rate of coarsening was derived on a bubble by bubble basis according to differences in interior pressures and these coars-

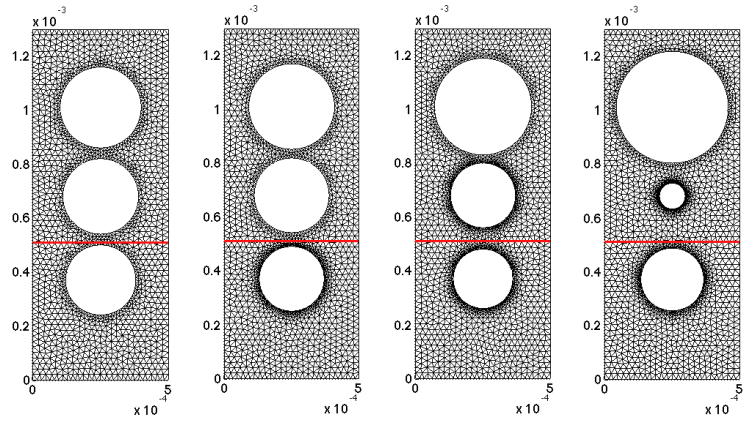

Figure 4.9: Time series depiction of the foam when varying film thicknesses are allowed: (a) 0 seconds, (b) 100 seconds, (c) 200 seconds, (d) 300 seconds. For reference, we include the line across which the drainage velocity is calculated.

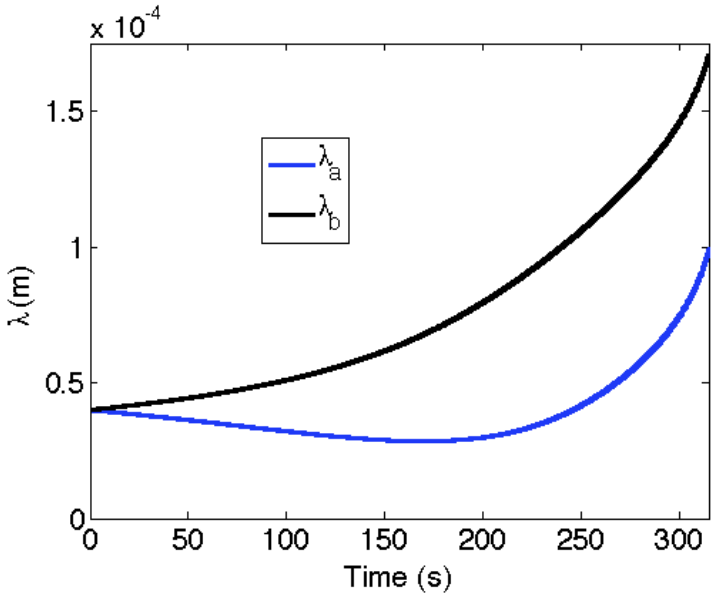

Figure 4.10: Film thicknesses over the course of 300 seconds when varying film thicknesses are allowed.

ening equations were used to specify the velocity of the moving bubble interfaces. Comparisons between our model's drainage results and experimental data suggest that allowing film thicknesses to vary within the coarsening equations results in a more accurate representation of local coarsening and drainage dynamics than con-

stant film thicknesses. Using our varying film thickness coarsening equations, we have also shown that both bubble size and position are important. Current coarsening theory would have Bubble 3, the smallest, disappearing first, but we have shown that Bubble 2 is the first to disappear. This suggests that bubble position needs to be accounted for in coarsening studies, both local and global.

In the next chapter, the algorithm's free body capabilities are investigated. Specifically, we are interested in the range of ρ_B values that can be captured by the model. Previous rigid particle, ALE works have been limited by the range of ρ_B values that can be explored. This investigation is based off of two tests, which are similar in nature to the terminal velocity validation test performed in Chapter 3. A cylinder, of density ρ_B, is submerged in water and the cylinder's dynamics are modeled using Equation 1.1 as the cylinder's boundary condition. After each successful simulation, ρ_B is changed such that the difference between ρ_B and ρ becomes progressively larger. This testing allows us to discern whether or not our algorithm has improved ρ_B capabilities over those of previous rigid particle ALE works. More importantly, this testing allows us to conclude whether or not we can reasonably expect the algorithm to be able to capture the free body dynamics of the droplets and bubbles that comprise micro-emulsions and micro-foams.

Chapter 5: Algorithm Capabilities

After successfully modeling the coarsening of an idealized foam and studying the local drainage that coarsening induces, we turn our attention to the modeling of free bodies. Our model captures the dynamics of free bodies by using Equations 1.1, 1.2, and 1.3 on the surfaces of the bodies. When using these equations, is our algorithm capable of treating the droplets and bubbles within micro-emulsions and micro-foams as free bodies? Our algorithm's ability to do so depends on its ability to capture a wide range of ρ_B values.

Looking at Equations 1.2 and 1.3, one can see that the density difference term is the driving force behind the motion of the free bodies. However, the ρ_B^{-1} coefficient attached to all of the terms in Equations 1.2 and 1.3 is just as important. When ρ_B becomes small, these coefficients can become large, which causes Equations 1.2 and 1.3 to become stiff in comparison to the incompressible Navier-Stokes equations. The effects of this stiffness have limited the range of ρ_B values that have been captured with a rigid particle ALE treatment. To determine whether our algorithm has increased ρ_B capabilities compared to those of previous rigid particle ALE works, we utilize two capability studies that are similar in nature to the final validation test.

Within the first capability study, a free body cylinder of fixed radius is submerged in a container of water and the fluid dynamics are modeled until the buoyant cylinder reaches its terminal velocity. After the completion of each simulation, the cylinder is given a smaller ρ_B value. This process of decreasing ρ_B continues until finding the cylinder's terminal velocity becomes prohibitively expensive. Once the simulation's cost becomes too large, the study is concluded and the algorithm's ρ_B limit, with respect to today's computing resources, is declared. Let the ρ_B limit of the first study be denoted as ρ_B^*.

The second capability study presumes that running the first study's simulations with $\rho_B < \rho_B^*$ will become cheaper to run with increased computing power in the future. The study begins where the first study concluded and its computing expenses are reduced by using a smaller domain than the first capability study. In addition, the second capability study's simulations are only run for several hundred timesteps. Similar to the first study, ρ_B is decreased after each successful simulation. Once an instability due to a decrease in ρ_B cannot be avoided, the overall limit of the algorithm, with respect to ρ_B and the study's domain, is declared. The limit results of these two capability studies are then used to answer the question of whether or not we will be able to model micro-foams and micro-emulsions as a collection of free bodies.

5.1 Capability Study I

The domain in this first study is identical to the one used in the terminal velocity validation test within Chapter 3. A cylinder, of radius 10^{-4} m, is placed along the centerline of the container and the container's width is such that $\xi = 10$. No-slip boundary conditions are placed on all four sides of the container. The height of the container and position of the cylinder are such that the container's top and bottom no-slip boundary conditions do not significantly affect the motion of the droplet. Equation 1.1 is applied to the buoyant cylinder's surface and after each successful simulation, the cylinder's density is decreased. The fluid's dynamic viscosity and density remain fixed at $10^{-3}\,{}^{\mathrm{kg}}/_{\mathrm{m\cdot s}}$ and $10^{3}\,{}^{\mathrm{kg}}/_{\mathrm{m}^3}$, respectively, throughout the entirety of the study.

No leaden cylinders are considered in this study because of our interest in determining whether or not we have an algorithm capable of capturing micro-foams and micro-emulsions as a collection of free bodies. In addition, unlike the previous terminal velocity study, there is no restraint placed upon the Re values that can be explored. Figure 5.1 is a plot of this test's results. Within Figure 5.1, the V_T predicted by Equation 3.10 is included for reference.

For $\rho_B \in [930, 1000]{}^{\mathrm{kg}}/_{\mathrm{m}^3}$, the numerical results for V_T match those predicted by Equation 3.10, as expected. Once ρ_B becomes less than $930{}^{\mathrm{kg}}/_{\mathrm{m}^3}$, the flow within the container exits the Stokes regime and the two V_T profiles diverge. The Stoke's assumption in Equation 3.10 leads to an under-prediction of the surface stress, see [3], which leads to Equation 3.10 over-predicting V_T. This over-prediction is

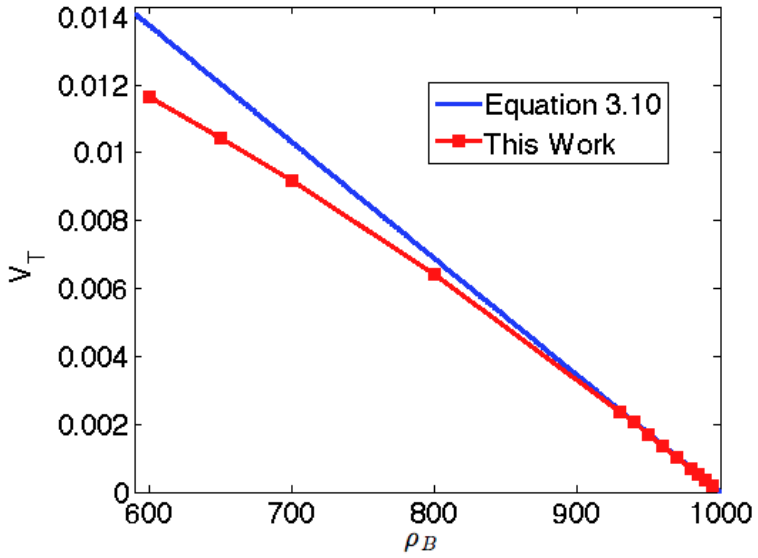

Figure 5.1: Terminal velocities of the buoyant cylinders we were able to capture within the restraints of our first capability study.

evident in Figure 5.1, however, Equation 3.10 remains an excellent estimate of V_T.

The largest density difference that we captured within this study was 400 $^{kg}/_{m^3}$, corresponding to $\rho_B = 600^{kg}/_{m^3}$. To put things in perspective, vegetable oil has a density of approximately $920^{kg}/_{m^3}$, diesel fuel has a density of approximately $800^{kg}/_{m^3}$, and butane has a density of approximately $550^{kg}/_{m^3}$ [8]. Modeling larger density differences required smaller Δt values, which would have necessitated smaller Δx values for the model's results to remain reliable. With this study's domain, a decrease in Δx would have led to computer memory issues. Regardless, these results are encouraging because many buoyant liquids, with respect to water, have $\rho_B \in [600, 1000]^{kg}/_{m^3}$. Of particular interest to us are the oils and fuels that are immiscible in water and form an emulsion with water in the presence of a stabilizer. The results of this first study suggest that our model is capable of studying

micro-emulsions of this type as a collection of free bodies.

5.2 The PE(CE)$^\infty$ Scheme and Equation 1.2

Densities smaller than $600\,{}^{\mathrm{kg}}/_{\mathrm{m}^3}$ were not possible in the first capability study because $\pm$ oscillations surfaced in the solution for $\vec{V}$ and smaller Δt values were not possible. Naturally, we question why these $\pm$ oscillations appeared and what restricted us from exploring larger density differences. To answer these questions, we analyze how the PE(CE)$^\infty$ scheme treats Equation 1.2.

We begin our analysis by focusing on a free body starting from rest, a condition that carries the utmost importance. When starting from rest, the stress term in Equation 1.2 is equivalent to zero in the first iteration of the PE(CE)$^\infty$ scheme. This is because there is no previous, nonzero velocity field upon which the algorithm can base its stress prediction. This results in $\vec{V}$ being predicted solely from the acceleration term within Equation 1.2. If Δt is not small enough, the cylinder's first predicted velocity can be large enough such that it is over-corrected in the following iteration. By over-correcting, we mean that the deceleration term is large enough that its magnitude outweighs that of the acceleration term.

When this over-correction occurs, $\vec{V}$ becomes negative. A series of alternating, ever increasing, positive and negative predictions for $\vec{V}$ occurs in the following iterations. To remove the $\pm$ oscillation, Δt must be decreased, but as we learned in the previous study, this is not always possible. If Δt cannot be decreased, the simulation cannot recover from these $\pm$ oscillations. However, that is not to say

that the PE(CE)$^\infty$ scheme is a poor choice for our algorithm.

To put the previous capability study's limit of $\rho_B = 600\,{}^{\text{kg}}/_{\text{m}^3}$ into perspective, Figure 5.2 contains the limits of previous rigid particle ALE fluid simulations. Since our reasoning indicates that Equation 1.2's acceleration term is the restriction term, the limits are plotted as a function of $\left|(\rho_B - \rho)\rho_B^{-1}\right|$. Figure 5.2 was made by assuming a ρ of $1000\,{}^{\text{kg}}/_{\text{m}^3}$ and taking the maximum values of ρ_B that were explicitly mentioned within the literature. Only the results for Newtonian fluid simulations were considered so that comparisons can be made between our limits and those of published works. The maximum $\left|(\rho_B - \rho)\rho_B^{-1}\right|$ value previously captured in a rigid particle, Newtonian fluid ALE simulation was that mentioned by [16], 0.5. Our successful simulation of $\rho_B = 600\,{}^{\text{kg}}/_{\text{m}^3}$ corresponds to a $\left|(\rho_B - \rho)\rho_B^{-1}\right|$ value of 0.667, which means that we have already extended the limits of $\left|(\rho_B - \rho)\rho_B^{-1}\right|$ in the first capability study.

We hope to achieve larger $\left|(\rho_B - \rho)\rho_B^{-1}\right|$ values in the next study, but before we attempt to do so, we turn our focus back to Figure 5.2. Interestingly enough, no buoyant particle simulations were carried out in [14–16]. With our previous reasoning showing that $(\rho_B - \rho)\rho_B^{-1}$ is the restricting quantity, can the sedimentation results of [14], [15], and [16] be reflected about ρ into the buoyant regime? To answer this, we further analyze the PE(CE)$^\infty$ scheme's treatment of Equation 1.2.

Consider two cylinders with identical areas, one with $\rho_B = 600\,{}^{\text{kg}}/_{\text{m}^3}$ and another with $\rho_B = 3000\,{}^{\text{kg}}/_{\text{m}^3}$. These values were chosen because $\rho_B = 600\,{}^{\text{kg}}/_{\text{m}^3}$ was the limit of our previous capability study and $\rho_B = 3000\,{}^{\text{kg}}/_{\text{m}^3}$ corresponds to the

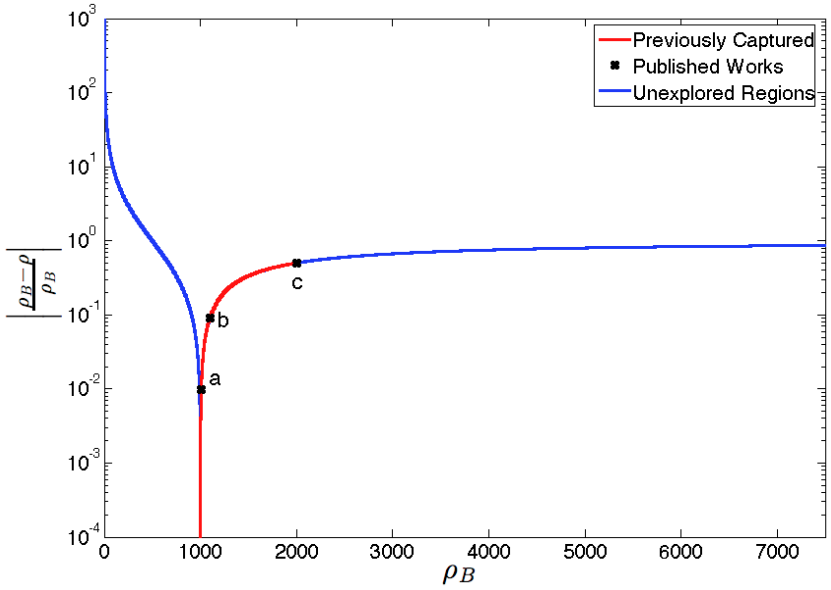

Figure 5.2: The $|(\rho_B - \rho)\rho_B^{-1}|$ limits of previous rigid particle ALE fluid simulations assuming $\rho = 1000\,\mathrm{kg/m^3}$. The letters next to the marks signifying values from published works (a, b, and c) refer to [15], [14], and [16] respectively.

same $\left|(\rho_B - \rho)\rho_B^{-1}\right|$ value, 0.667. After starting from rest, the initial predicted velocities of the cylinders will be identical in size because of their matching acceleration terms. Thus, their stress forces will be identical in the following corrector step, but their deceleration terms will differ. This is because the deceleration term is calculated as the product of the stress force and $(\rho_B A_B)^{-1}$. This means that compared to the simulation with $\rho_B = 600\,\mathrm{kg/m^3}$, the $\rho_B = 3000\,\mathrm{kg/m^3}$ simulation will have a damped deceleration.

A damped deceleration decreases the possibility of over-correction and this allows for density ratios larger than 0.667 to be captured in leaden simulations without having to change Δt. This implies that while $(\rho_B - \rho)\rho_B^{-1}$ remains the primary restricting quantity with regards to our algorithm's capabilities, the $(\rho_B A_B)^{-1}$ term causes the $(\rho_B - \rho)\rho_B^{-1}$ restriction to be asymmetric about ρ. Because the $(\rho_B - \rho)\rho_B^{-1}$

restriction is asymmetric about ρ, the results of [14], [15], and [16] cannot be translated to the buoyant regime.

Since the previous study's domain was essentially arbitrary and computer resources are ever increasing, we choose to run another capability study. In it, we test our algorithm's abilities with regard to ρ_B values smaller than $600\,{}^{\mathrm{kg}}/_{\mathrm{m}^3}$ and we test its stability when running simulations with these ρ_B values. The previous study's computer memory issues are avoided by using a smaller domain. In addition, this study's simulations are only run for 250 timesteps. When it comes to determining the stability of the algorithm, 250 timesteps are sufficient because $\pm$ oscillations make themselves present well before even 50 timesteps have elapsed. Both of these changes make this investigation more economical when using our current computing resources.

5.3 Capability Study II

For this study, ξ, ρ, μ, and the cylinder's radius remain unchanged from the previous study. This is done for two reasons. First, when it comes to ρ, μ, and r_B, we want to remain in the range of values that one would expect to encounter in micro-foams and micro-emulsions. Second, and more importantly, we want to be able to compare this study's results to those of the previous study as well as those of previous works. If the wall effects or area of the cylinder were to differ, comparison would not be possible. Unlike the previous study, both leaden and buoyant cylinders are modeled in this study to explore the asymmetry of $\left|(\rho_B - \rho)\rho_B^{-1}\right|$.

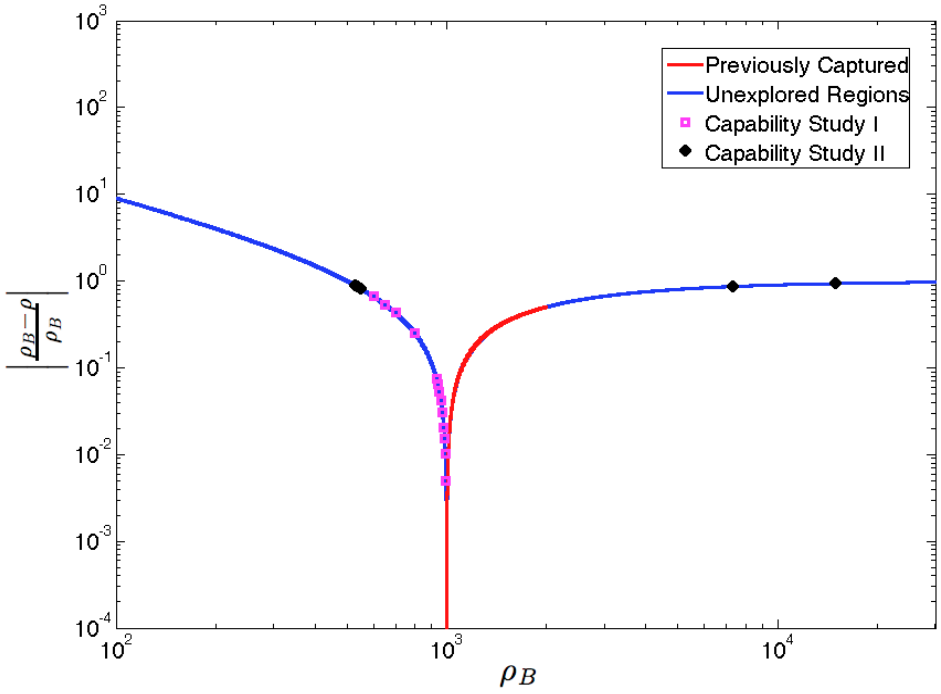

Figure 5.3: The $|(\rho_B-\rho)\rho_B^{-1}|$ limits of this work. The results from the first capability study are included for reference.

Figure 5.3 contains the results of this study, the results of the previous study, and the range of limits from the literature. Several aspects of Figure 5.3 need mentioning. To begin, the lowest value of ρ_B we were able to capture with our algorithm was $530\,{}^{\mathrm{kg}}/_{\mathrm{m}^3}$, which corresponds to a $\left|(\rho_B-\rho)\rho_B^{-1}\right|$ value of approximately 0.887. This means that treating a micro-foam as a collection of free body bubbles is not feasible with our algorithm unless smaller cylinders are considered and computing power is significantly increased. However, this does not mean that micro-foams cannot be studied with this model (e.g. coarsening of an idealized foam).

Second, our leaden restrictions are less severe than the buoyant regime's restriction of $\left|(\rho_B-\rho)\rho_B^{-1}\right| = 0.887$. With our algorithm, a maximum ρ_B of $15000\,{}^{\mathrm{kg}}/_{\mathrm{m}^3}$ was explored. This ρ_B value is close to the density of mercury, see [8], and it approx-

imately corresponds to a $\left|(\rho_B - \rho)\rho_B^{-1}\right|$ value of 0.93. In terms of $\left|(\rho_B - \rho)\rho_B^{-1}\right|$, this means that our algorithm's capabilities extend 86% beyond the capabilities of previous works. In terms of ρ_B, this equates to an almost 15 times larger range of values when $\rho = 1000\,{}^{\text{kg}}/_{\text{m}^3}$. The difficulties encountered when simulating $\rho_B = 530\,{}^{\text{kg}}/_{\text{m}^3}$ were not encountered during the $\rho_B = 15000\,{}^{\text{kg}}/_{\text{m}^3}$ simulations. In fact, the simulations became relatively easy for these large values of ρ_B. Larger values of ρ_B could have been explored, but were not because we felt that $\rho_B = 15000\,{}^{\text{kg}}/_{\text{m}^3}$ sufficiently demonstrated our algorithm's potential when it comes to leaden cylinder simulations.

The discrepancy in the maximum $\left|(\rho_B - \rho)\rho_B^{-1}\right|$ values we captured on either side of ρ are indicative of the asymmetry that the $(\rho_B A_B)^{-1}$ term causes. To support our previous reasoning, we devise a simple numerical experiment to test whether or not the $(\rho_B A_B)^{-1}$ term is responsible for restricting the algorithm's ρ_B capabilities instead of the $(\rho_B - \rho)\rho_B^{-1}$ term. If $(\rho_B A_B)^{-1}$ were the restricting term, the algorithm's ρ_B limits would be contingent upon the magnitude of $(\rho_B A_B)^{-1}$. This would imply that as long as $(\rho_B A_B)^{-1}$ remained the same or decreased in size, we should be able to explore smaller values of ρ_B by increasing A_B. For our algorithm's limit of $\rho_B = 530\,{}^{\text{kg}}/_{\text{m}^3}$, with $r_B = 10^{-4}$ m, the quantity $(\rho_B A_B)^{-1}$ is approximately equal to $60058\,{}^{\text{m}}/_{\text{kg}}$. When $r_B = 1.02 * 10^{-4}$ m^2 and $\rho_B = 520\,{}^{\text{kg}}/_{\text{m}^3}$, the quantity $(\rho_B A_B)^{-1}$ is approximately 60013. Since $60058 > 60013$, $\rho_B = 520\,{}^{\text{kg}}/_{\text{m}^3}$ could be captured if $r_B = 1.02 * 10^{-4}$ m^2 and $(\rho_B A_B)^{-1}$ were the restricting term. Testing this setup within the model proved otherwise. Despite a smaller $(\rho_B A_B)^{-1}$, $\pm$ oscillations ap-

peared in the $\vec{V}$ solution for $\rho_B = 520\,{}^{\text{kg}}/_{\text{m}^3}$. This confirms the importance of the $(\rho_B - \rho)\rho_B^{-1}$ term as our algorithm's restricting term.

5.4 Chapter Conclusions

Within this chapter, we have investigated the free body capabilities of our algorithm. Specifically, we have investigated the range of ρ_B values that our algorithm can capture. Our investigation showed that our algorithm is capable of modeling the free body dynamics of cylinders with densities between $530\,{}^{\text{kg}}/_{\text{m}^3}$ and $15000\,{}^{\text{kg}}/_{\text{m}^3}$ when $\rho = 1000\,{}^{\text{kg}}/_{\text{m}^3}$. Analysis showed that the limits encountered by our rigid particle ALE algorithm are caused by the magnitude of the $(\rho_B - \rho)\rho_B^{-1}$ term in Equation 1.2. In addition, analysis showed that the $(\rho_B A_B)^{-1}$ term in Equation 1.2 is responsible for the asymmetry of the algorithm's $\left|(\rho_B - \rho)\rho_B^{-1}\right|$ limit about ρ.

Even though our algorithm is limited by today's computing power, it is capable of capturing an 86% larger range of $\left|(\rho_B - \rho)\rho_B^{-1}\right|$ values than previous rigid particle, Newtonian fluid ALE works. When $\rho = 1000\,{}^{\text{kg}}/_{\text{m}^3}$, this equates to an almost 15 times larger range of ρ_B values than was previously possible. We attribute our algorithm's capabilities to the PE(CE)$^\infty$ scheme. While we have significantly extended the capabilities of rigid particle ALE simulations with respect to $\rho_B > \rho$, we are more interested in our algorithm's capabilities with respect to the buoyant regime.

Our testing has shown that we will be unable to capture micro-foams as a collection of free bodies. This is due to our algorithm's lowest current ρ_B limit of

$530\,{}^{\mathrm{kg}}/_{\mathrm{m}^3}$. However, these results indicate that we should be able to capture micro-emulsions as a collection of free bodies. When it comes to micro-emulsions, we are interested in studying water and liquid fuel mixtures. Since most liquid fuels have densities in the range of $700\,{}^{\mathrm{kg}}/_{\mathrm{m}^3}$ to $950\,{}^{\mathrm{kg}}/_{\mathrm{m}^3}$ and because these densities lie within our algorithm's capabilities, we hope to be able to study drainage from micro-emulsions with our algorithm in the future. From these micro-emulsion drainage studies, we may be able to extend their results to include drainage in micro-foams.

In the next and final chapter, we will conclude this dissertation.

Chapter 6: Conclusions

We have created an ALE model and algorithm for the purpose of studying multiphase flows. Unlike many of the algorithms and models within the current multiphase literature, our algorithm takes a heterogeneous approach, which allows us to resolve the local flows that homogeneous media models ignore. The ALE method's ability to easily handle the heterogeneous treatment's moving interfaces made it an obvious choice for our model, however, ALE simulations are more expensive to run than their fixed grid counterparts. To reduce simulation costs, without jeopardizing the ALE method's ability to handle moving interfaces, we based our algorithm on a second order accurate, semi-implicit-explicit time integration scheme. Timestep analysis of this scheme and the scheme's application to the weak form of the incompressible, Navier-Stokes ALE equations were presented in Chapter 2. In addition, Chapter 2 discussed a novel function designed for controlling the grid deformation that takes place during Laplacian smoothing.

In Chapter 3, we validated our algorithm and its implementation against analytical and empirical expressions in several studies. These validation studies not only confirmed our algorithm's ability to accurately resolve flow fields and predict the dynamics of free bodies, but they also confirmed our algorithm's second order

accuracy. After thoroughly validating our algorithm, we studied the coarsening of an idealized micro-foam in Chapter 4. The idealized micro-foam was designed to be similar to those studied by Kennedy et al. and equations governing the coarsening rate of each of its bubbles, $\frac{dR_i}{dt}$, were derived. With this study, it was shown that varying film thicknesses need to be taken into account in future coarsening models and it was also shown that a bubble's position is as important as its size when it comes to the process of coarsening.

Our investigations ended with a series of algorithm capability studies in Chapter 5. These studies showed that our model is capable of capturing an 86% larger range of $\left|(\rho_B - \rho)\rho_B^{-1}\right|$ values than previous rigid particle ALE models, which equates to an almost 15 times larger range of ρ_B values. Although the capability studies showed that treating a micro-foam as a collection of free body bubbles is not within our algorithm's abilities, they did indicate that treating a micro-emulsion as a collection of free body droplets is within our model's abilities.

In the near future, we hope to use this ALE model to study global drainage from micro-emulsions. We believe that global drainage, or the liquid that escapes from the bottom of a foam or emulsion, is due to an imbalance of the buoyancy and capillarity forces. Our drainage study in Chapter 4 only investigated a foam's internal drainage, but the increases in film thickness and decreases in surface area depicted by Figures 4.9d and 4.10 suggest that such an imbalance does occur. Studying the effects of this imbalance requires the model to be capable of capturing a collection of free bodies. Although micro-foams are out of our reach, the results of Chapter 5 suggest that a study of a micro-emulsion's global drainage is possible with

our ALE model. Furthermore, it may be possible to extend the micro-emulsion's global drainage results to include global drainage from a micro-foam. However, if that is not possible, algorithm modifications may be considered so a ρ_B smaller than $530\,{}^{\mathrm{kg}}/_{\mathrm{m}^3}$ can be captured by the model.

Appendix A: Derivation of Local Coarsening Equations for Poly-Disperse Bubbles

To determine the coarsening equations for Bubbles 1, 2, and 3, we begin with Bubble 2. From conservation of mass,

$$\pi R_1^2 L_B + \pi R_2^2 L_B + \pi R_3^2 L_B = constant, \tag{A.1}$$

it can be shown that

$$\frac{dR_2}{dt} = -\frac{R_1}{R_2}\frac{dR_1}{dt} - \frac{R_3}{R_2}\frac{dR_3}{dt}, \tag{A.2}$$

where R_1, R_2, and R_3 are the radii of Bubbles 1, 2, and 3, respectively. Equation A.2 represents the coarsening equation for Bubble 2. To determine the equations for Bubbles 1 and 3, we employ the well accepted assumption that gas is only transported between neighboring bubbles by means of diffusion. Thus, gas cannot be transported from Bubble 1 to Bubble 3 without first moving through Bubble 2 and the change in a bubble's volume with respect to time can be equated to the volumetric, diffusive flux.

Starting with Bubble 1, which has area A_1 and constant length L_B in our 2D model, we write

$$\frac{d(A_1 L_B)}{dt} = A_a V_m D_f \frac{dc_a}{d\lambda_a} \tag{A.3}$$

where A_a is the apparent area between Bubbles 1 and 2, V_m is the molar volume constant, D_f is the diffusion coefficient for dissolved gas in water, c_a is the concentration of dissolved gas in the water between Bubbles 1 and 2, and λ_a is the distance between Bubbles 1 and 2. In Equation A.3 we have already specified the diffusive flux to be one dimensional. We further simplify matters by using the common coarsening approximation of

$$D_f \frac{dc_a}{d\lambda_a} \approx D_f \frac{\Delta c_a}{\lambda_a}. \tag{A.4}$$

The quantity λ_a is now understood to be the minimum distance between Bubbles 1 and 2 and Δc_a is specified to be the change in the concentration of dissolved gas from Bubble 2's interface, c_2, to Bubble 1's interface, c_1. Henry's law states that the ratio of the dissolved gas's concentration to the bubble's interior pressure, P, is a constant, He. This implies that $c_2 = HeP_2$ and $c_1 = HeP_1$. The interior pressures can be specified as $P_1 = \gamma R_1^{-1}$ and $P_2 = \gamma R_2^{-1}$ by using the Young-Laplace equation, where γ represents surface tension. This means that we have

$$c_1 = \frac{He\gamma}{R_1} \tag{A.5}$$

and

$$c_2 = \frac{He\gamma}{R_2}, \tag{A.6}$$

as well as

$$c_3 = \frac{He\gamma}{R_3} \tag{A.7}$$

by following similar logic for Bubble 3. From Equations A.5 and A.6, it can be seen that since $R_1 > R_2$, we have $c_1 < c_2$. This implies that gas diffuses from Bubble 2

to Bubble 1 according to

$$D_f \frac{dc_a}{d\lambda_a} \approx \frac{D_f}{\lambda_a}\Big(\frac{He\gamma}{R_2} - \frac{He\gamma}{R_1}\Big). \tag{A.8}$$

This phenomenon of larger bubbles growing at the expense of smaller bubbles has been recognized in previous coarsening works and it forms the basis of coarsening theory [13, 17, 26].

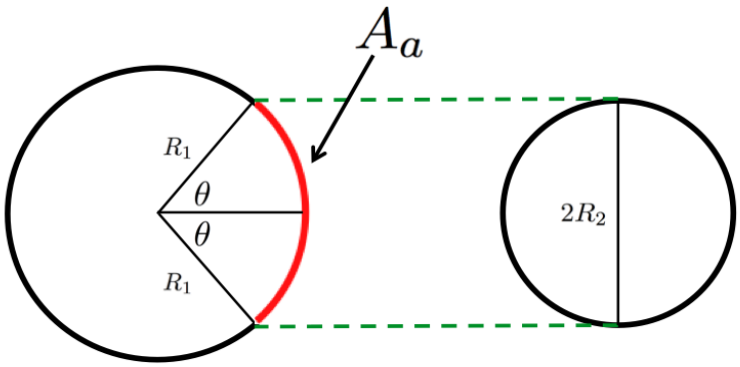

Figure A.1: Apparent area, A_a, according to Bubble 1's view factor of Bubble 2.

The second feature of Equation A.3 we wish to discuss is A_a. The apparent area, A_a, is related to the theory of view factors and it governs the area through which gas can be accepted by Bubble 1 from Bubble 2. A_a is determined by the projection of Bubble 2 onto Bubble 1 and it can be seen in Figure A.1 as the red portion of Bubble 1's surface. Figure A.1 is a 2D depiction and it should be understood that the area implied by A_a is calculated as the product of the highlighted arc length with the length of the cylinder, L_B. This leads us to the expression

$$A_a = 2\theta R_1 L_B, \tag{A.9}$$

where θ can be written in terms of R_1 and R_2 using the arcsin function. The final expression for A_a is

$$A_a = 2R_1 L_B \sin^{-1}\left(\frac{R_2}{R_1}\right). \tag{A.10}$$

By inserting Equations A.8 and A.10 into Equation A.3, the equation

$$\frac{dR_1}{dt} = \left(\frac{V_m D_f He\gamma}{\lambda_a}\right)\left(\frac{\sin^{-1}\left(\frac{R_2}{R_1}\right)}{\pi}\right)\left(\frac{1}{R_2} - \frac{1}{R_1}\right) \tag{A.11}$$

can be derived. It is important to remember that within the derivation of Equation A.10, and thus Equation A.11, the relationship $R_1 > R_2$ was utilized.

The equation governing the rate of change in Bubble 3's volume with respect to time is very similar to that of Bubble 1's and is written as

$$\frac{d(A_3 L_B)}{dt} = A_b V_m D_f \frac{dc_b}{d\lambda_b}. \tag{A.12}$$

The diffusive flux for Bubble 3 is written as

$$D_f \frac{dc_b}{d\lambda_b} \approx \frac{D_f}{\lambda_b}\left(\frac{He\gamma}{R_2} - \frac{He\gamma}{R_3}\right), \tag{A.13}$$

where c_b is the concentration of dissolved gas in the water between Bubbles 2 and 3 and λ_b is understood to be the minimum distance between Bubbles 2 and 3. For $R_2 > R_3$, the apparent area governing the transport of gas between Bubbles 2 and 3, A_b, can be written as

$$A_b = 2R_2 L_B \sin^{-1}\left(\frac{R_3}{R_2}\right) \tag{A.14}$$

by using a similar derivation to that of A_a. By inserting Equations A.13 and A.14 into Equation A.12, the equation

$$\frac{dR_3}{dt} = \left(\frac{V_m D_f He\gamma}{\lambda_b}\right)\left(\frac{\sin^{-1}\left(\frac{R_3}{R_2}\right)}{\pi}\right)\left(\frac{1}{R_3} - \frac{R_2}{R_3^2}\right) \tag{A.15}$$

results. It is important to remember that within the derivation of Equation A.14, and thus Equation A.15, the relationship $R_2 > R_3$ was utilized.

Now, within current coarsening literature, it is assumed that the film thicknesses are equal to $3.5 * 10^{-8}$m for all times [17]. On the local scale, there is little evidence suggesting that the film thicknesses should be $3.5 * 10^{-8}$m, let alone constant, and it is not unreasonable to expect them to change with time as the bubble sizes change with time. To determine whether constant film thicknesses or varying film thicknesses are more appropriate, two sets of equations are built from Equations A.2, A.11, and A.15.

The first set of equations corresponds to constant film thicknesses and is built by replacing the film thicknesses λ_a and λ_b in Equations A.11 and A.15 with ε. Then, the quantities $V_m D_f He\gamma(\varepsilon)^{-1}$ in Equations A.11 and A.15 are collapsed into a constant, effective diffusion coefficient, D [17]. Thus, the first set of coarsening equations are

$$\frac{dR_1}{dt} = D\left(\frac{\sin^{-1}\left(\frac{R_2}{R_1}\right)}{\pi}\right)\left(\frac{1}{R_2} - \frac{1}{R_1}\right), \tag{A.16}$$

$$\frac{dR_2}{dt} = -\frac{R_1}{R_2}\frac{dR_1}{dt} - \frac{R_3}{R_2}\frac{dR_3}{dt}, \tag{A.17}$$

and

$$\frac{dR_3}{dt} = D\left(\frac{\sin^{-1}\left(\frac{R_3}{R_2}\right)}{\pi}\right)\left(\frac{1}{R_3} - \frac{R_2}{R_3^2}\right). \tag{A.18}$$

When calculating D, the values used for V_m, D_f, He, γ, and ε are $0.0245\,{}^{\mathrm{m}^3}/_{\mathrm{mol}}$, $2.6 * 10^{-9}\,{}^{\mathrm{m}^2}/_{\mathrm{s}}$, $6.2 * 10^{-6}\,{}^{\mathrm{mol}}/_{\mathrm{m}^3\cdot\mathrm{Pa}}$, $0.03\,{}^{\mathrm{N}}/_{\mathrm{m}}$, and $3.5 * 10^{-8}$m, respectively [17]. When these values are used, D is comparable to the effective diffusion coefficients determined

empirically by Kennedy et al..

For the second set of equations, we consider time dependent λ_a and λ_b by multiplying D with the ratio of the initial film thicknesses, λ_a^0 and λ_b^0, to the time dependent film thicknesses, λ_a and λ_b. Our simulations are obviously not on the nanometer scale and it is almost absurd for us to have fixed ε to be $3.5 * 10^{-8}$m within the first set of equations. However, by modifying D in this fashion, changes in λ_a and λ_b can be reflected without having to simulate on the nanometer scale. The resulting set of equations are

$$\frac{dR_1}{dt} = \left(\frac{D\lambda_a^0}{\lambda_a}\right)\left(\frac{\sin^{-1}\left(\frac{R_2}{R_1}\right)}{\pi}\right)\left(\frac{1}{R_2} - \frac{1}{R_1}\right), \tag{A.19}$$

$$\frac{dR_2}{dt} = -\frac{R_1}{R_2}\frac{dR_1}{dt} - \frac{R_3}{R_2}\frac{dR_3}{dt}, \tag{A.20}$$

and

$$\frac{dR_3}{dt} = \left(\frac{D\lambda_b^0}{\lambda_b}\right)\left(\frac{\sin^{-1}\left(\frac{R_3}{R_2}\right)}{\pi}\right)\left(\frac{1}{R_3} - \frac{R_2}{R_3^2}\right). \tag{A.21}$$

There are no differences between Equations A.17 and A.20, the equations that enforce mass conservation within our system.

Now, remember that when deriving Equation A.21, it was assumed that $R_2 > R_3$. We have found that this is not always the case in our simulations. When varying film thicknesses are considered, it is possible for Bubble 3 to become larger than Bubble 2 despite being initially smaller than Bubble 2. When $R_3 > R_2$, Equation A.21 must be replaced by

$$\frac{dR_3}{dt} = \left(\frac{D\lambda_b^0}{\lambda_b}\right)\left(\frac{\sin^{-1}\left(\frac{R_2}{R_3}\right)}{\pi}\right)\left(\frac{1}{R_2} - \frac{1}{R_3}\right). \tag{A.22}$$

Equation A.22 can be found using a derivation similar to that of Equation A.11.

Bibliography

[1] Ascher, U., Ruuth, S., and Wetton, B., "Implicit-Explicit Methods for Time-Dependent Partial Differential Equations". SIAM Journal of Numerical Analysis, 32 (3), 797-823, 1995.

[2] Bouard, R. and Coutanceau, M., "Étude Théorique et Expérimentale de l'Écoulement Engendré par un Cylindre en Translation Uniforme dans un Fluide Visqueux en Régime de Stokes". Journal of Applied Mathematics and Physics, 37, 673-684, 1986.

[3] Bird, R., Stewart, W., Lightfoot, E., *Transport Phenomena Second Edition.* John Wiley and Sons, Inc., 2007.

[4] Deen, W., *Analysis of Transport Phenomena: Second Edition.* Oxford University Press, Inc., 2012.

[5] Dennis, S. and Shimshoni, M., "The Steady Flow of a Viscous Fluid Past a Circular Cylinder". Her Majesty's Stationery Office, 797, 1-48, 1965.

[6] Donea, J., Giuliani, S., and Halleux, J., "An Arbitrary Lagrangian-Eulerian Finite Element Method for Transient Dynamic Fluid-Structure Interactions". Computer Methods in Applied Mechanics and Engineering, 33, 689-723, 1982.

[7] Donea, J., Huerta, A., Ponthot, J., and Rodríguez-Ferran, A., "Arbitrary Lagrangian-Eulerian Methods". *Encyclopedia of Computational Mechanics.* John Wiley & Sons, Inc., 2004.

[8] Elert, G., *The Physics Hypertextbook.* Web, 25 March 2015.

[9] Feng, J., Hu, H., and Joseph, D., "Direct Simulation of Initial Values Problems for the Motion of Solid Bodies in a Newtonian Fluid Part 1. Sedimentation". Journal of Fluid Mechanics, 261, 95-134, 1994.

[10] Formaggia, L. and Nobile, F., "Stability Analysis of Second-Order Time Accurate Schemes for ALE-FEM". Computer Methods in Applied Mechanics and Engineering, 193, 4097-4116, 2004.

[11] Ghosh, S. and Stockie, J. "Numerical Simulations of Particle Sedimentation Using the Immersed Boundary Method". Submitted to Journal of Computational Physics.

[12] Gunzburger, M., *Finite Element Methods for Viscous Incompressible Flows: A Guide to Theory, Practice, and Algorithms*. Academic Press, Inc., 1989.

[13] Hilgenfeldt, S., Koehler, S., and Stone, H., "Dynamics of Coarsening Foams: Accelerated and Self-Limiting Drainage". Physical Review Letters, 86 (20), 4704-4707, 2001.

[14] Hu, H., "Direct Simulations of Flows of Solid-Liquid Mixtures". International Journal of Multiphase Flow, 22 (2), 335-352, 1996.

[15] Hu, H., Joseph, D., and Crochet, M., "Direct Simulation of Fluid Particle Motions". Theoretical and Computational Fluid Dynamics, 3, 285-306, 1992.

[16] Hu, H., Patankar, N., and Zhu, M., "Direct Numerical Simulations of Fluid-Solid Systems Using the Arbitrary Lagrangian-Eulerian Technique". Journal of Computational Physics, 169, 427-462, 2001.

[17] Kennedy, M., Conroy, M., Dougherty, J., Otto, N., Williams, B., Ananth, R., and Fleming, J., "Bubble Coarsening Dynamics in Fluorinated and non-Fluorinated Firefighting Foams". Colloids and Surfaces A: Physicochemical and Engineering Aspects, Accepted 2015.

[18] Larson, M., and Bengzon, F., *The Finite Element Method: Theory, Implementation, and Applications*. Springer, 2013.

[19] Liu, J., "Simple and Efficient ALE Methods with Provable Temporal Accuracy up to Fifth Order for the Stokes Equations on Time Varying Domains". SIAM Journal of Numerical Analysis, 51 (2), 743-772, 2013.

[20] Liu, K., Lu, Y., and You, C., "High-Order ALE Method for the Navier-Stokes Equations on a Moving Hybrid Unstructured Mesh using Flux Reconstruction Method". International Journal of Computational Fluid Dynamics, 27 (6-7), 251-267, 2013.

[21] Minion, M. and Brown, D., "Performance of Under-Resolved Two-Dimensional Incompressible Flow Simulations, II". Journal of Computational Physics, 138, 734-765, 1997.

[22] Shewchuk, J., "What Is a Good Linear Finite Element?: Interpolation, Conditioning, Anisotropy, and Quality Measures". Preprint, 2002.

[23] Shyy, W., Udaykumar, S., Rao, M., and Smith, R., *Computational Fluid Dynamics with Moving Boundaries*. Dover Publication, Inc., 1996.

[24] Soulaimani, A. and Saad, Y., "An Arbitrary Lagrangian-Eulerian Finite Element Method for Solving Three-Dimensional Free Surface Flows". Computer Methods in Applied Mechanics and Engineering, 162, 79-106, 1998.

[25] Takaisi, Y., "Note on the Drag on a Circular Cylinder Moving with Low Speeds in a Viscous Liquid Between Two Parallel Walls". Journal of the Physical Society of Japan, 11 (9), 1009-1013, 1956.

[26] Vera, M., and Durian, D., "Enhanced Drainage and Coarsening in Aqueous Foams". Physical Review Letters, 88 (8), 2002.

[27] Yue, P., Feng, J., Bertelo, C., and Hu, H., "An Arbitrary Lagrangian-Eulerian Method for Simulating Bubble Growth in Polymer Foaming". Journal of Computational Physics, 226, 2229-2249, 2007.